Quarterly Report for

October - December 1999

Stanford Geothermal Program

DE-FG07-99ID13763

Table of Contents

1. MEASUREMENTS OF STEAM-WATER RELATIVE PERMEABILITY

This research project is being conducted by Research Assistant Peter O'Connor, Research Associate Kewen Li and Professor Roland Horne. The aim is to measure relative permeability relations for steam and water flowing simultaneously in rock and to examine the effects of temperature, flow rate, and rock type. In the first stage, the experiments will attempt to reproduce results obtained in a previous experiment (Mahiya, 1999), but holding the experimental pressure as close as possible to a constant value.

1.1 BACKGROUND

An X-ray CT technique has been used in recent years to measure the distribution of steam and water saturation in rocks to obtain steam-water relative permeability curves (Satik and Horne, 1998, Mahiya, 1999). Glenn Mahiya conducted his experiment in 22 steps with imbibition and drainage processes across a range of saturation conditions. The resulting relationship for steam-water relative permeability as a function of saturation resembled a Corey function. Since the mass flow rate was almost constant, and since the process was adiabatic but not isothermal, it was difficult to maintain a constant pressure differential. Variations in pressure cause changes in the slip factor, which may have contributed to scatter in the steam relative permeability curve. A new experiment will attempt to maintain a constant pressure, to avoid this difficulty.

1.2 EXPERIMENTAL PROCEDURE

A Berea sandstone core will be subjected to 120E C in an oven while simultaneously pulling a vacuum on it. A dry X-ray scan is made to obtain CT_{dry}. The core is then fully saturated with water and scanned to obtain CT_{wet}. From these, a porosity distribution will be obtained, expected to yield an average value of 24.7%. In the next step, hot liquid water is flowed through to obtain CT_{hw}, which is necessary to calculate experimental saturations. The next steps are the actual flow-through experiments. The core will be under a pressure gradient of approximately 6-8 psi across the 41-cm length. First, the core is saturated with steam. Steam flow rate will be gradually lowered in 10% increments, to implement an imbibition process whereby the wetting phase (water) displaces the nonwetting phase (steam). A flexible heat guard ensures negligible overall heat loss for a near-adiabatic process. At each step, the system will reach a steady state and will then be subject to CT scan to measure saturation. Steam flow rate will be reduced to 0%, then increased. This second sequence will be a drainage sequence.

At every stage, pressure, temperature and heat fluxes from the core are to be measured. Calculated relative permeability to steam and water are then plotted against the saturation measurements. The major suggested change from the previous experiment is to perform the imbibition step first. Performing the imbibition step first allows determination of the maximum pressure. This pressure can be maintained by increasing flow rates if necessary.

1.3 EXPERIMENTAL DESIGN

The experimental equipment follows that used previously by Mahiya, as shown in Figure 1.1.

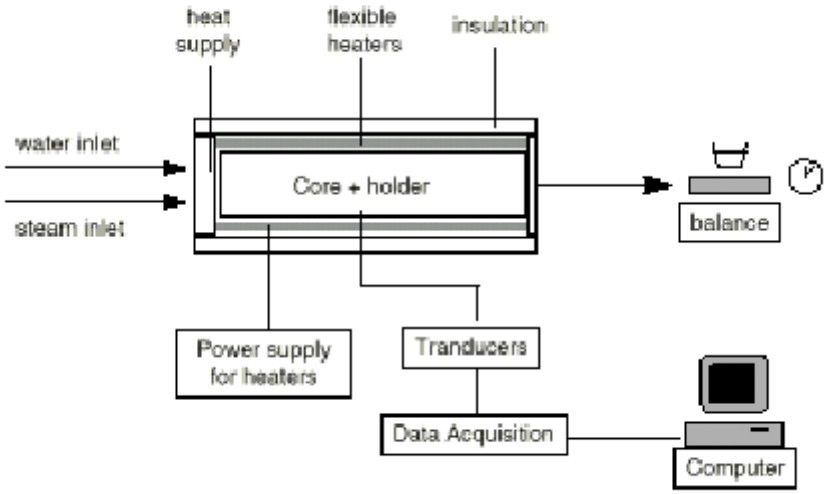

Figure 1.1: Schematic of steam-water flow apparatus.

1.4 FUTURE RESEARCH

This project intends to develop into investigation of the steam-water relative permeability relationship in Geysers rocks. Due to the extremely low permeability of such rock, concerns arise regarding the time required to run the experiment, especially if a number of separate trials are required as in the original experimental method. In addition, unusual difficulties may arise such as increased boundary capillary effect due to the necessarily short core sample. The method best for measuring relative permeability in sandstone cores may or may not be the best method for measuring the same in Geysers rock.

2. AN EXPERIMENTAL INVESTIGATION OF BOILING HEAT CONVECTION WITH RADIAL FLOW IN A FRACTURE

This project is being conducted by Research Assistant Robb Barnitt and Professor Roland Horne. The goal is to investigate and compare the heat flux and temperature gradients that develop during boiling with liquid injection into a simulated rock fracture. Ultimately, this project intends to develop a boiling convection coefficient for use in calculating heat transfer with boiling in fractured geothermal rock. Improved understanding and modeling of heat transfer in a fracture will lead ultimately to better strategies for injection into fractured geothermal reservoirs.

2.1 INTRODUCTION

Work conducted this quarter included a rerun of the aluminum disk experiment and graywacke disk experiment preparations. This experiment was rerun with the goal of obtaining better results than were generated in the previous run. Additional work involved preparing a disk of graywacke to fit the experimental apparatus. The next experiment will utilize this rock, obtained from a Geysers core.

2.2 ALUMINUM DISK EXPERIMENT RERUN

2.2.1 Experimental Conditions

The experimental procedure employed in the repeat of this experiment was nearly identical to the original method, with a few exceptions. Data were collected with the outer edge of the apparatus exposed to atmospheric pressure. The fracture was oriented horizontally and a small positive displacement pump was used to pump water through a copper coil immersed in boiling water to provide fluid near saturated temperature. The pump was adjusted to supply discrete rates of 15, 30, and 45 ml/min, and the fracture aperture was fixed at 0.508 mm. With liquid water these rates are well within the range of laminar flow. With boiling, however, the velocity was further increased as liquid flashed to vapor in the fracture. Eight 1.0 mm diameter T-type thermocouples installed previously in the aluminum disk at varying distances from the fracture surface, recorded the temperature gradients that develop as water flashes to steam in the fracture. Calculation of the boiling convection coefficient requires that the surface temperature (T_{surf}), on the top of the aluminum disk and in the fracture, be known. This was calculated previously by linear interpolation of the linear temperature gradient which developed axially in the aluminum disk. To achieve a tangible value of T_{surf}, thin 12.5 micron thick cementable thermocouples were purchased and installed. Three such thermocouples were attached to the fracture surface using a cement of high thermal conductivity, spaced 120 degrees apart, and oriented 1.5 cm from the disk center.

During this experiment 95 volts and about 2.5 amps were supplied to the heater and were maintained at those levels for the duration of the entire experiment. Temperatures were recorded every minute for many hours while the flow rate was adjusted and the times of steady state conditions were noted.

2.2.2 Experimental Results

This experiment produced temperature gradients and heat fluxes on the order of those recorded in the previous experiment. However, there were some dissimilarities.

As has occurred previously, the heat flux sensors provided results that we suspect are incorrect. In the previous experiment, the heat flux sensors failed at approximately 10,000 W/m^2. In this experiment, they registered on the order of 7,000 W/m^2 for the duration of the experiment. However, based upon calculations utilizing the measured voltage and current delivered to the heater, a heat flux of approximately 38 kW/m^2 was delivered to the aluminum disk. Furthermore, implementing Fourier's Law of heat conduction and considering the temperature gradient across the middle of the aluminum disk, and an assumed thermal conductivity of 237 W/mK, the heat flux can be calculated as approximately 20 kW/m^2. Taking into account the efficiency factor of the heater, and the fact that the assumption of one-dimensional heat conduction is not entirely accurate, this value seems plausible. These calculations cast some doubt over the reliability of the heat flux sensor data. Therefore, the heat flux q'' was calculated using the measured temperature gradient across the middle of the aluminum disk.

This experiment utilized the new cementable thermocouples, adhered to the surface of the aluminum (i.e. the fracture wall). It was hoped that these surface thermocouples would provide tangible data previously determined from linear extrapolation of the temperature gradient within the aluminum. However, the temperatures recorded by these surface thermocouples was several degrees below saturation temperature, as well as below the anticipated T_{surf} value determined from linear extrapolation. Values of T_{sat} and T_{surf} were used to determine the excess temperature (T_e). A negative value of T_e was calculated when the surface thermocouple data is used. A positive, and therefore acceptable, value of T_e was calculated when using the T_{surf} suggested by the linear extrapolation.

Using the values for q'' and T_e, as described above, a boiling convection coefficient h can be determined for each flow rate.

$$h = q'' / T_e$$

$$[W / m^2 K] \equiv [(W / m^2) / (K)]$$

A comparison of results achieved in both aluminum disk experiments are presented in Table 2.1. A graphical comparison of the calculated h for each of the aluminum disk experiments, as well as the sandstone experiment, is presented in Figure 2.1.

Table 2.1: Aluminum disk results comparison

	January, 1999			December 1999		
Flow Rates	15 ml/min	30 ml/min	60 ml/min	15 ml/min	30 ml/min	45 ml/min
T_{sat} (^oC)	100.22	99.63	99.65	99.27	100.44	100.05
T_{surf} (^oC) [1]	101.56	100.10	98.68	100.84	101.76	101.45
T_{surf} (^oC) [2]	NM	NM	NM	94.29	97.07	96.63
T_e (K) [1]	1.34	0.47	-0.97	1.57	1.32	1.40
T_e (K) [2]	NM	NM	NM	-4.98	-3.37	-3.43
q" (W/m^2)	27,437	28,470	32,331	21,877	20,386	22,316
h (W/m^2K)	20,489	61,185	NM	13,951	15,475	15,990

[1] Utilized data extrapolated from linear temperature trend across center of disk.

[2] Utilized measured data from cementable surface thermocouples.

NM = Not Measured

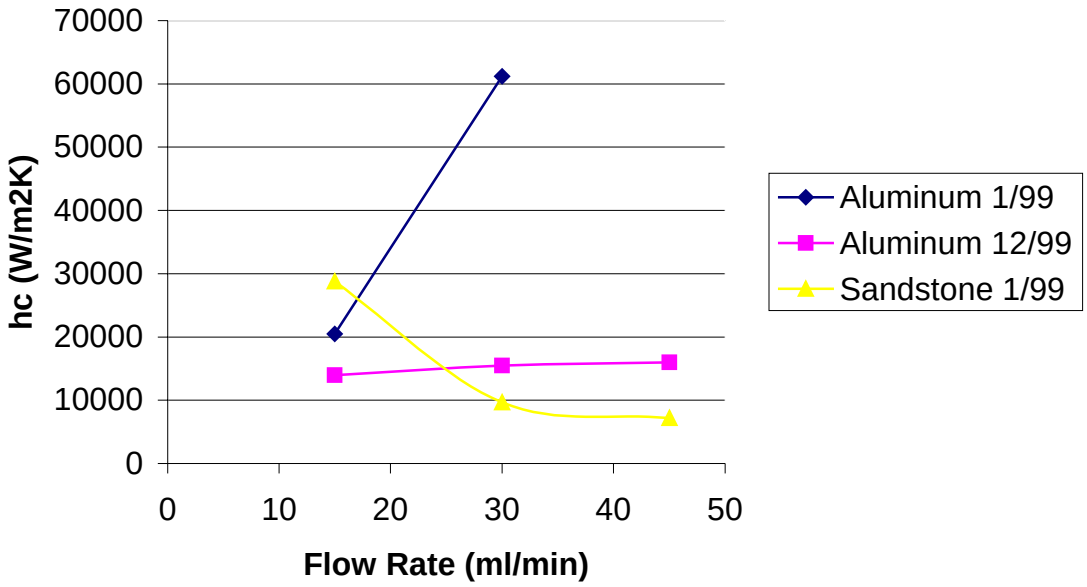

Figure 2.1: Comparison of h for each experiment.

It is apparent from this comparison that several trends differ between the experiments. For this reason, the aluminum disk experiment will be run once again.

2.3 GRAYWACKE DISK PREPARATION

Using a diamond-tipped rock saw, two portions of graywacke were cut from a 3 1/4 inch diameter core sample. Each disk was cut to approximately 2 cm in width. Each side was rendered flat and parallel to the other with the use of a surface grinder. The sample proved to be fairly brittle, and was subject to some fracturing and breakage at the radial edge during both phases of the preparation. This should not affect the experimental data

as the thermocouples obtain data from an axial plane 1.5 cm from the center of the disk. The drilling of thermocouple holes has not yet been achieved since the hardness of the rock requires the requisition of a special drill bit.

2.4 FUTURE WORK

The previously executed experiment using the aluminum disk will be redone. The cemented surface thermocouples will be recalibrated prior to the experiment. It is possible that the foil leads of the thermocouples may have contacted the glass disk during the experiment, perhaps altering their results. Additionally, as a potential precursor to an experimental procedure to employ in the upcoming graywacke experiment, several power levels will be used at each of the flow rates. These additional data points may be used to refine the accuracy of the subsequent boiling convection coefficient calculations.

New, harder drill bits have been ordered for installing the thermocouple holes in the graywacke disk. After these holes have been drilled, and the aluminum disk experiment repeated, the apparatus will be reconfigured to accept the smaller graywacke disk. Then the graywacke experiment can be completed.

3. INFERRING ENDPOINT AND IN-SITU WATER SATURATION FROM LABORATORY AND FIELD MEASUREMENTS

This project is being conducted by Research Assistant Rodolfo Belen Jr., Research Associate Kewen Li and Prof. Roland Horne. The aim is to infer the endpoint saturation of steam and liquid water relative permeability curves of geothermal reservoir rocks as well as the in-situ water saturation of geothermal reservoirs from laboratory and field measurements.

3.1 INTRODUCTION

Relative permeability is important in describing the flow of two-phase steam in geothermal reservoirs. Presently, however, relative permeability relations for steam and liquid water are not completely understood. Permeability relations are normally adopted from field data or from nitrogen and water flow experiments.

The experimental determination of steam and liquid water relative permeabilities is a central target of the Stanford Geothermal Program. Flow-through experiments on Berea sandstones were performed by Ambusso (1996), Satik (1998) and Mahiya (1999) that utilized X-ray computer tomography to determine steam saturation profiles. In a different approach, numerical simulation was used by Guerrero et al. (1998) to infer relative permeabilities of Berea sandstones, based on temperature, pressure, and steam saturation data obtained from steady state boiling experiments performed by Satik (1997).

All of these earlier studies used Berea sandstone in order to capitalize on its higher permeability relative to geothermal rocks, which enabled the experiments to be performed in reasonable time. This study aims to extend the understanding to low permeability geothermal rocks by determining only the endpoint saturations of the relative permeability curves. The endpoint or irreducible or immobile saturation of a certain phase is the saturation at which that phase becomes mobile in multiphase flow.

Combining information about the endpoint saturations from the “slow” geothermal rock experiments with information about the general shape of the relative permeability curves from the “faster” sandstone rock experiments will completely define the steam-liquid water relative permeability behavior.

Furthermore, determination of the endpoint and in-situ water saturation will provide a better understanding of the adsorption characteristics and fluid storage capacities of geothermal rocks. This will be valuable in accurately estimating the size of the available resource in vapor-dominated reservoirs as well as liquid-dominated reservoirs that are experiencing dry out as a result of exploitation.

The objective of this study is to determine the endpoint saturation of the steam and liquid water relative permeability curves by inference from pressure, temperature and saturation data obtained from previous boiling experiments conducted in Berea sandstone cores. Furthermore, this study aims to determine the feasibility of performing the boiling experiments using Geysers geothermal rocks.

This study also aims to develop a model that will allow inference of the in-situ water saturation and, if possible, the endpoint water saturation from field measurements of temperature and production enthalpy. It is also the objective of this study to determine the feasibility of performing flash experiments using Berea sandstone and Geysers geothermal cores to determine the endpoint water saturation experimentally as well as to confirm the field techniques.

3.2 INFERRING ENDPOINT WATER SATURATION FROM BOILING EXPERIMENTS

Results of previous steady state boiling experiments performed by Satik (1997) were analyzed to investigate whether endpoint saturations can be inferred from the experimental data obtained.

3.2.1 Experimental Design of Boiling Experiments Using Berea Sandstone Cores

In 1996 and 1997, Satik performed a series of boiling experiments using Berea sandstone cores. The objective of the study was to further the understanding of the boiling process in porous media and ultimately to obtain capillary pressure functions and relative permeability relations for steam and liquid water. The steady state boiling experiments involved the heating of a rock saturated with liquid water and observing the boiling process by continuous measurement of pressure, temperature, heat flux and steam saturation within the rock. The X-ray CT scanner was used to visualize the boiling process and to determine the three-dimensional fluid distributions within the rock. The experimental apparatus (Figure 3.1) and procedure were described in detail in the Spring 1999 quarterly report.

The boiling experiments are analogous to drainage experiments in oil and water systems, in which oil, the non-wetting fluid, is injected into a rock saturated with water, the wetting fluid, to displace the water from the rock. However, in this case, steam produced by heating the water-saturated rock displaces the liquid water from the rock.

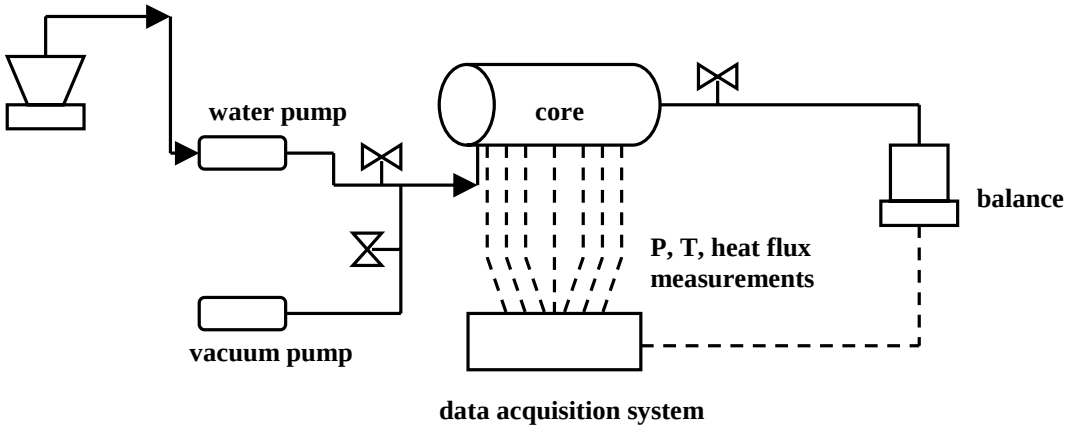

Figure 3.1: Configuration of boiling experiments.

3.2.2 Results of Boiling Experiments

It was observed that as the heating rate was increased, the steady state steam saturation profile indicated a progressive boiling process with the formation of distinct regions of steam, two-phase and liquid water. Figure 3.2 is the steam saturation profile of a vertical boiling experiment performed by Satik (1997) showing the formation of steam, two-phase and liquid regions within the core as the heating rate is increased. The sudden drop in the steam saturation near the heater end of the core that marks the transition from steam to two-phase conditions is designated here as the elbow in the saturation profile.

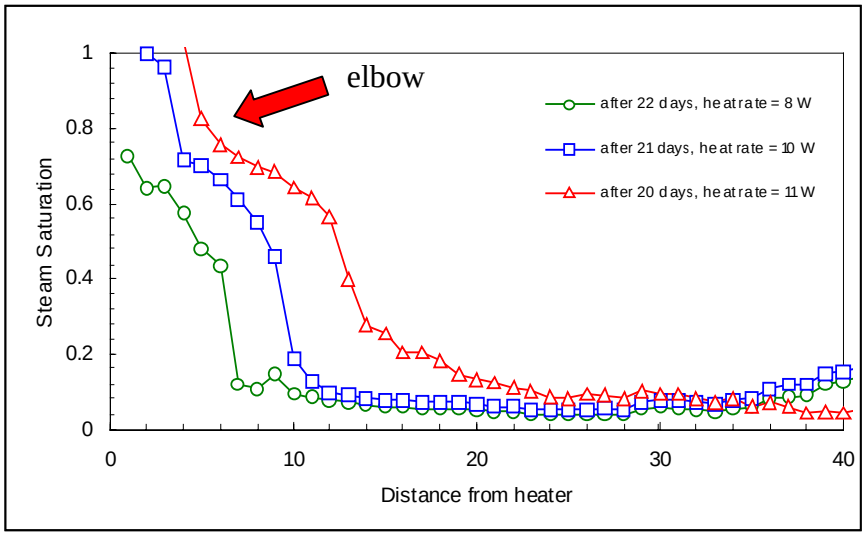

Figure 3.2: Steam saturation profile of vertical boiling experiment (Satik, Spring 1997).

3.2.3 Sensitivity Analysis of Boiling Experiments

It is hypothesized that the irreducible water saturation can be correlated with the observed elbow in the steam saturation profile. Analyzing the sensitivity of the boiling process to the irreducible water saturation through numerical modeling will test the validity of this hypothesis. The boiling process was simulated using different values of the endpoint water saturation of the relative permeability curves. The pressure, temperature and saturation profiles were predicted to verify if the elbow in the saturation profiles could be correlated with the irreducible water saturation.

In 1998, Guerrero et al. developed a two-dimensional radial iTOUGH2 model to infer relative permeability relations from the results of the boiling experiments. The same model was used in the sensitivity analysis but the grids were refined to give a better resolution of the variations in the steam saturation near the heater end of the core.

Forward calculations in iTOUGH2 were performed to predict the pressure, temperature, and steam saturation profiles along the core. It is assumed that linear steam-liquid water relative permeability functions and Leverett capillary functions govern the flow of two-phase steam in the sandstone core.

The nonadiabatic boiling process was simulated using varying heating rates as illustrated in Figure 3.3 and using three different values of endpoint water saturation: 0.1, 0.2, and 0.5. Steam saturation was then plotted at 0.2-cm. intervals and up to a distance 5 cm. away from the heater end. The profiles at various times are shown in Figures 3.4 to 3.6.

It is evident from the plots that the steam and two-phase regions expand as the heating rate is increased and as time progresses. As the heating rate is increased, boiling commences and steam and two-phase regions form.

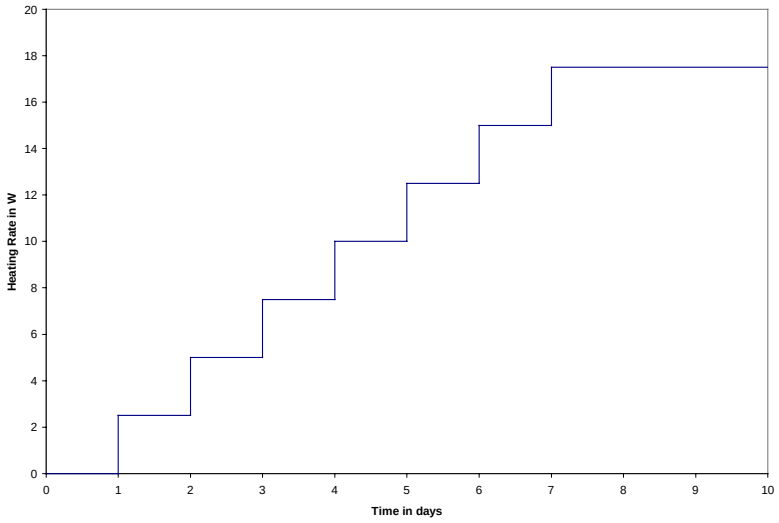

Figure 3.3: Variable heating rate profile.

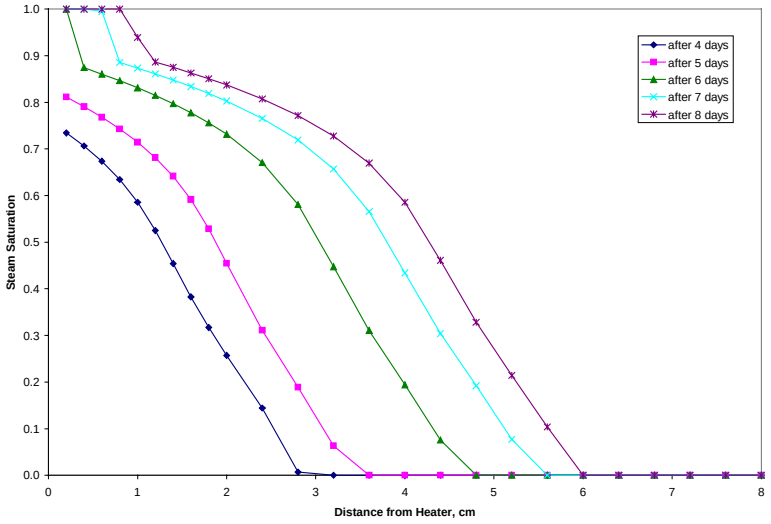

Figure 3.4: Steam saturation profile: endpoint water saturation = 0.1.

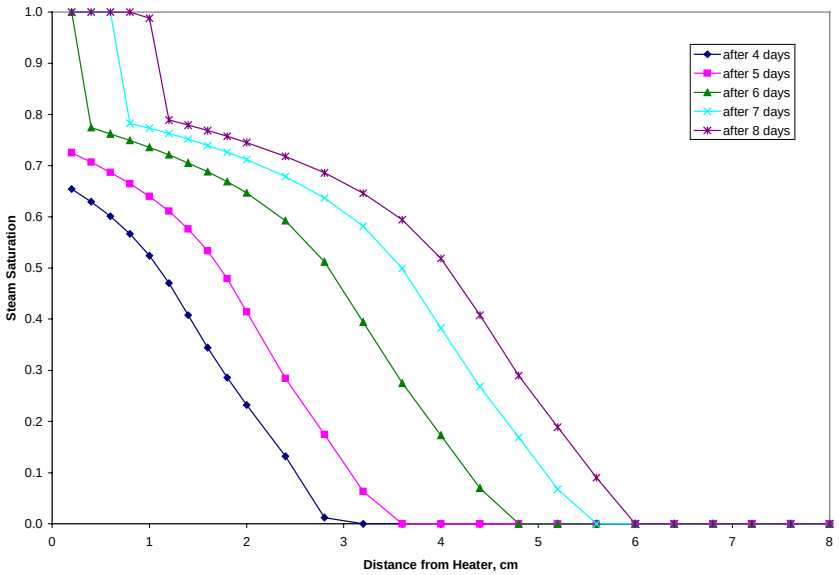

Figure 3.5: Steam saturation profile: endpoint water saturation = 0.2.

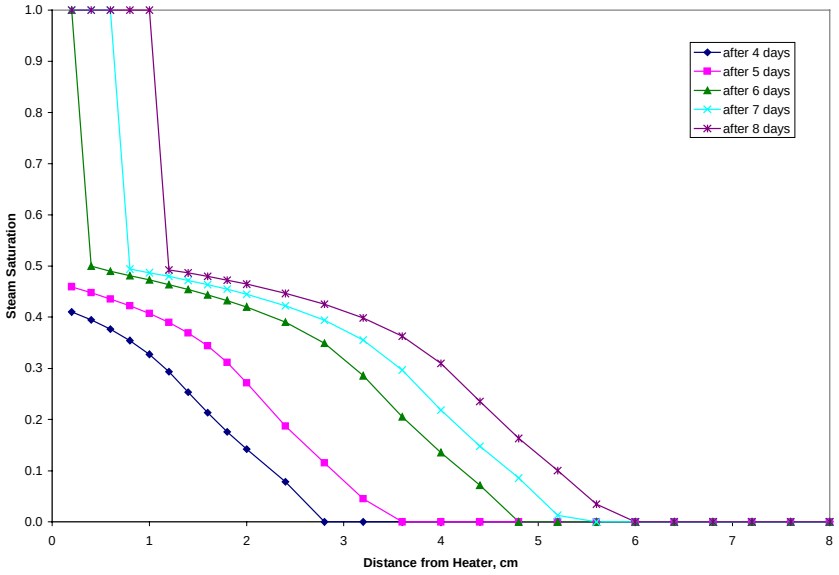

Figure 3.6: Steam saturation profile: endpoint water saturation = 0.5.

The simulation results indicate a correlation between the elbow in the steam saturation profile and the endpoint water saturation. In all three cases, the steam region extends to a distance one centimeter from the heater end. An abrupt drop in the steam saturation to a value close to the assumed endpoint water saturation marks the transition to two-phase conditions. This drop in steam saturation corresponds to the elbow in the profile. The steam saturation stays close to this value behind the elbow and then further goes down with distance away from the heater end.

It is important to note that steady state conditions were reached after about ten days of heating the core. Steady state means that the simulated steam saturation, pressure and temperature profiles remain invariant with time. As a consequence, the simulated steam saturation profiles indicate steam conditions in the region starting from the heater end to a distance one centimeter away. Beyond this region, the simulated steam saturation profiles indicate two-phase and liquid conditions.

3.2.4 Inferred Endpoint Water Saturation of Berea Sandstone Cores

Figures 3.2, and 3.7 to 3.9 show the steam saturation profiles obtained from the boiling experiments that were conducted by Satik in Spring and Summer 1997. The figures show the steam saturation profile with distance along the core and as a function of the heating rate. It is important to note that steam saturation, pressure and temperature were measured only at 1-cm intervals along the core.

It can be inferred from the experimental results that the irreducible water saturation of Berea sandstone is about 0.2. This inference is based on the observed elbow in the steam saturation profiles.

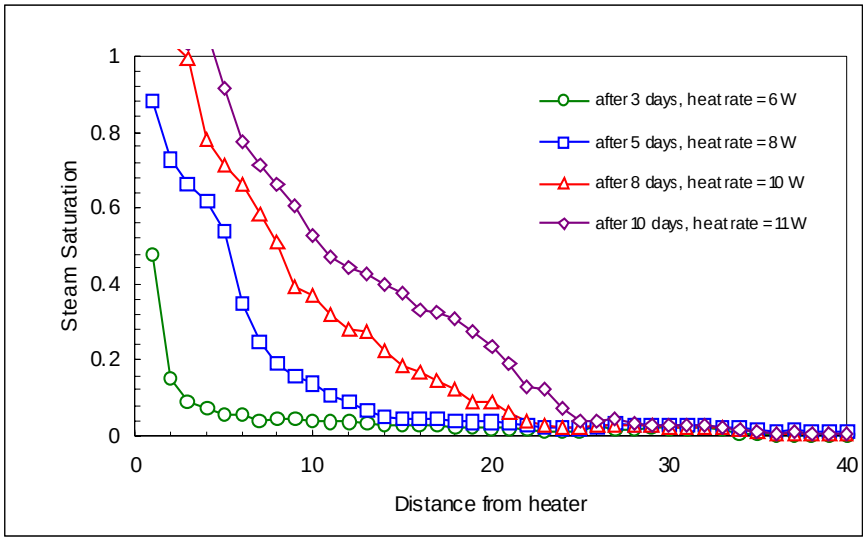

Figure 3.7: Steam saturation profile of horizontal boiling experiment (Satik, Summer 1997).

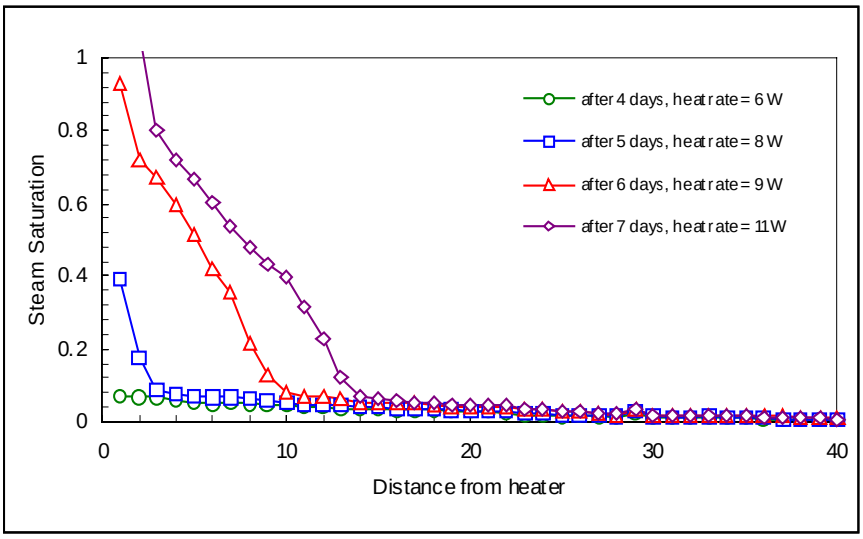

Figure 3.8: Steam saturation profile of top-heating vertical boiling experiment (Satik, Summer 1997).

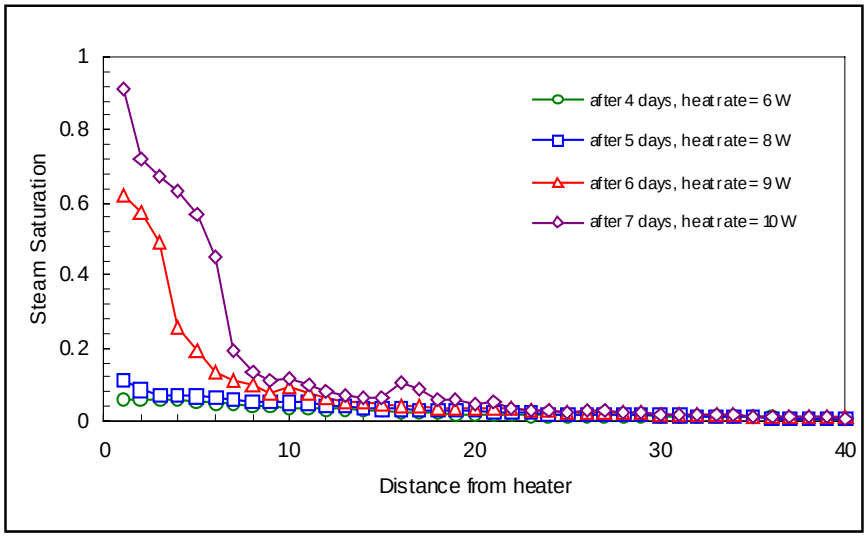

Figure 3.9: Steam saturation profile of bottom-heating vertical boiling experiment (Satik, Summer 1997).

3.2.5 Modeling Results of Boiling Experiments Using Geysers Geothermal Rocks

The boiling experiments were then modeled using Geysers geothermal rocks. The properties of the geothermal rocks used in the simulation runs are tabulated in Table 3.1.

As done previously in the Berea sandstone case, the nonadiabatic boiling process was simulated using constant and variable heating rates. Figures 3.10 and 3.11 show the steam saturation profiles with distance and heating rate. The plots correspond to the profiles after one day of continuously heating the core.

Table 3.1: Geysers geothermal rock properties.

Porosity	**5%**
Permeability	9×10^{-14} m^2
Rock density	2600 kg/m^3
Rock specific heat	485 J/kg°C
Rock heat conductivity	2.43 W/m°C

It is evident from the simulation results that the steam and two-phase regions expand as the heating rate is increased. However, it is important to note that in the case of the lower-porosity and lower-permeability geothermal rocks, the two-phase region is much shorter and the boiling front is much sharper relative to the Berea sandstone case, the results of which were reported in the Spring 1999 quarterly report. Consequently, the elbow in the steam saturation profile is less conspicuous in the Geysers case.

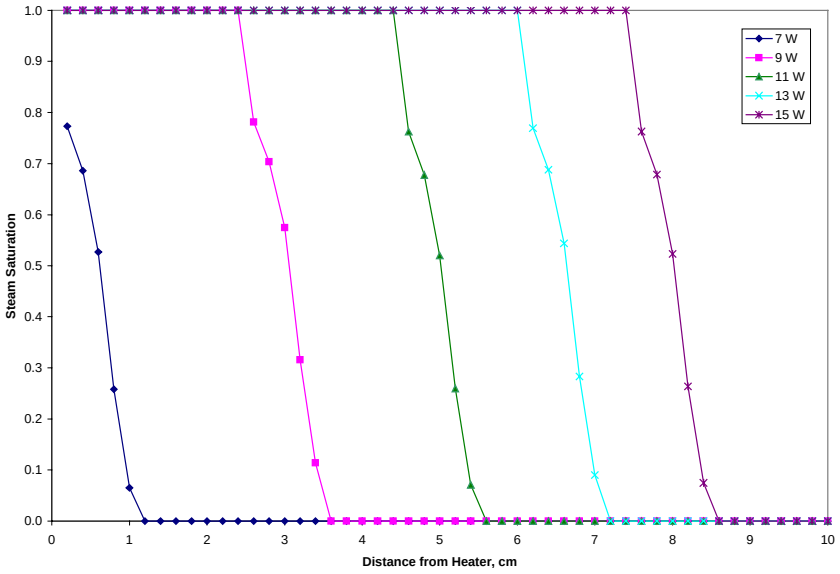

Figure 3.10: Steam saturation profiles with distance and constant heating rate, endpoint water saturation = 0.2.

Figures 3.12 to 3.14 show the simulation results when variable heating rates are used. The same heating rate profile is used in the modeling, which is shown in Figure 3.3. Likewise, steam and two-phase regions form and expand as the boiling process progresses. As expected, the two-phase region covers only a shorter distance and the boiling front is sharper. As a result, it is difficult to identify an elbow in the steam saturation profile. This very important simulation result must be taken into consideration in planning and designing boiling experiments in tighter and less permeable geothermal reservoir rocks. The difficulty in identifying the elbow in the steam saturation profile

may limit the usefulness of this approach in determining the endpoint water saturation of geothermal rocks from laboratory data obtained from boiling experiments.

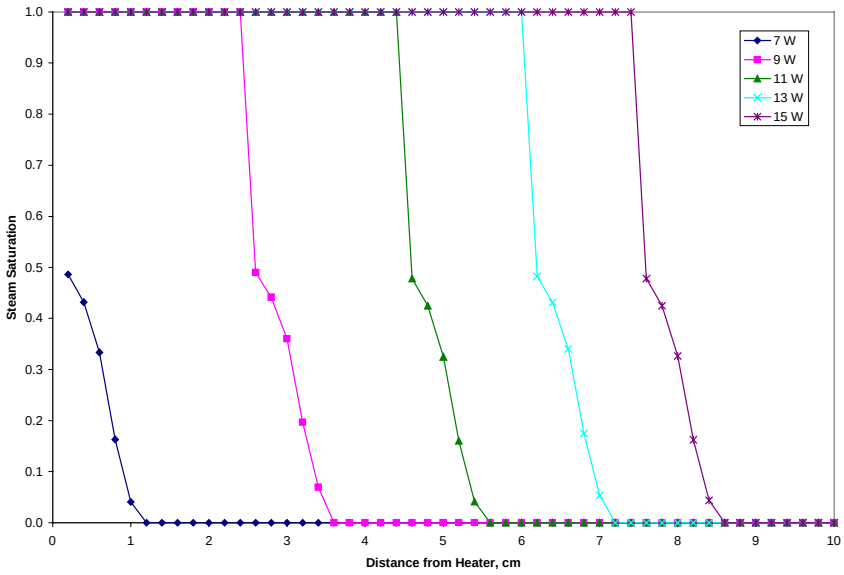

Figure 3.11: Steam saturation profiles with distance and constant heating rate, endpoint water saturation = 0.5.

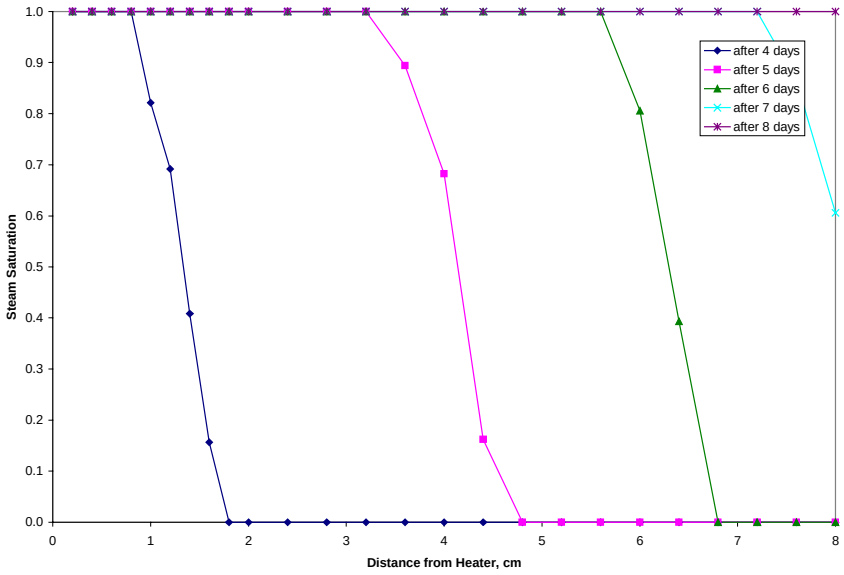

Figure 3.12: Steam saturation profiles with distance and time using variable heating rates, endpoint water saturation = 0.1.

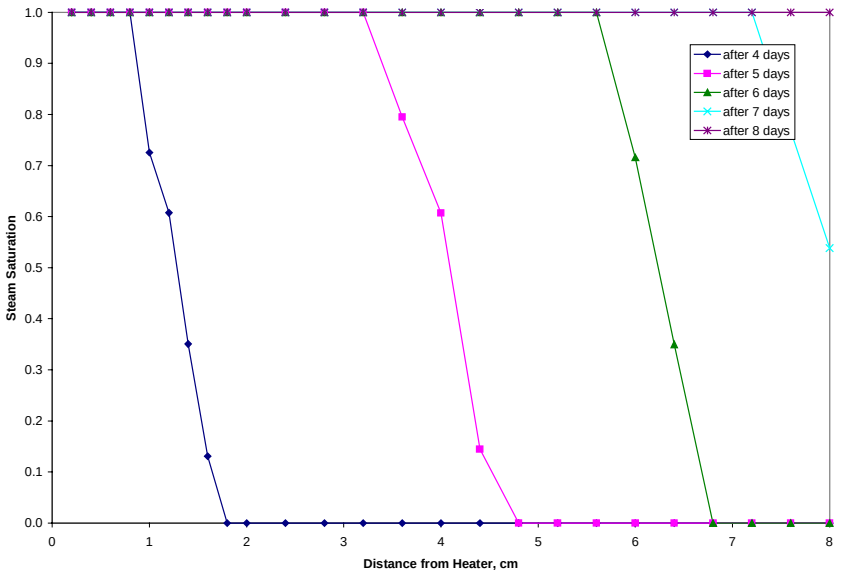

Figure 3.13: Steam saturation profiles with distance and time using variable heating rates, endpoint water saturation = 0.2.

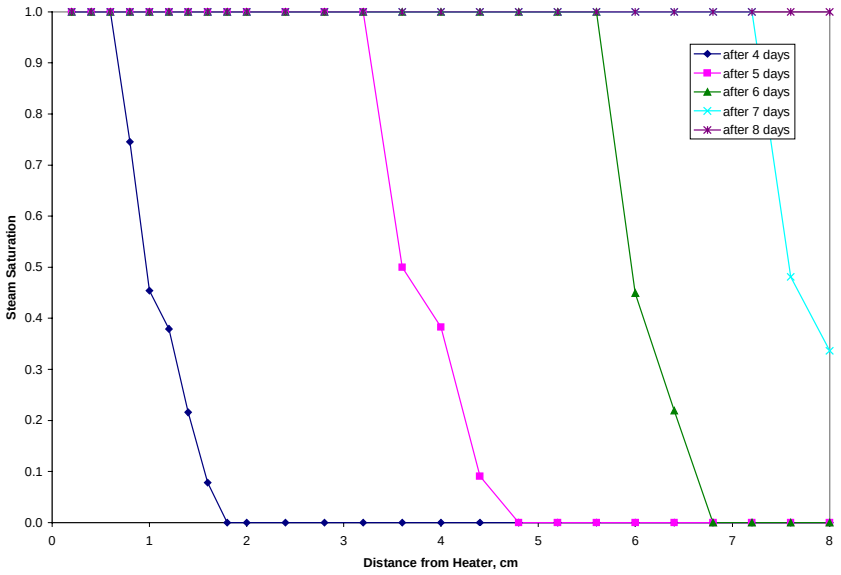

Figure 3.14:. Steam saturation profiles with distance and time using variable heating rates, endpoint water saturation = 0.5.

3.3 INFERRING IN-SITU WATER SATURATION FROM FIELD MEASUREMENTS

Steam production during the exploitation of vapor-dominated geothermal reservoirs greatly exceeds what the reservoir can store as vapor. Therefore, these reservoirs must contain substantial amounts of liquid water to sustain production (James, 1968;

Nathenson, 1975; Grant, 1979). In describing the response of vapor-dominated reservoirs to exploitation, it is valid to assume that the liquid water is completely immobile. Although water may be slightly mobile in the natural state of the reservoir, it is soon immobile because the water saturation drops as fluids are produced (Grant, 1979). The liquid water is adsorbed in the pores of the reservoir matrix and is able to vaporize, but is not able to flow as liquid water.

Grant (1979) estimated the in-situ water saturation of the Kawah Kamojang geothermal reservoir based on variations in the gas content of the production fluids. Changing the flow rate at the wellhead produces a response in the reservoir pressure and gas content, which allows for the estimation of the in-situ water saturation or the endpoint water saturation of the reservoir rock for this case of a vapor-dominated reservoir. In contrast, this study aims to infer the in-situ water saturation and, possibly, the endpoint saturation from field measurements of changes in the flowing enthalpies and production rates of producing wells.

Flow and lumped-parameter models can be used to describe the pressure, temperature and saturation distributions accompanying production. In the Spring 1999 quarterly report, the flow model used by Grant to infer the in-place water saturation of the Kawah Kamojang geothermal reservoir was presented. This study aims to develop a model that will be used to infer the in-situ and endpoint water saturations using field production data.

3.3.1 Future Work

Future work will be directed toward developing a model that will be used to infer in-situ and endpoint water saturations using field production data. Currently, a zero-dimensional model can be employed to estimate the in-situ water saturation based on material and energy balance equations. Future work will involve modeling of two-phase radial flow to obtain pressure and saturation profiles with time and radial distance. The modeling results will provide a deeper insight on the problem by confirming if the zero-dimensional model is sufficient or if it is necessary to extend the model to account for pressure and enthalpy variations with time and distance.

Furthermore, it is intended to extend the model to liquid-dominated reservoirs that produce two-phase steam. The goal is to extrapolate the in-situ and endpoint water saturations of the reservoir rocks using field production data.

3.4 INFERRING ENDPOINT WATER SATURATION FROM FLASH EXPERIMENTS

Flash experiments were modeled in TOUGH2 to determine if the endpoint water saturation can be inferred from experimental data.

3.4.1 Experimental Design of Flash Experiments

The flash experiment basically involves depressurizing a core initially saturated with liquid water and allowing the water to flash to atmospheric pressure. The experimental

apparatus will be similar to that of the boiling experiment performed by Satik, the configuration of which is shown in Figure 3.1. The apparatus will consist of a core holder housing the core, a data acquisition system, a vacuum pump, a water pump, a condenser and a balance. The core will be insulated with a fiber blanket to minimize heat losses. One end of the core will be attached to a water reservoir, which will be the source of water to saturate the core. The other end will be connected to a condenser and another water reservoir placed on a balance that will be used to monitor the amount of water or condensed steam produced from the core during the flash process. A backpressure regulator attached to the outlet end will be used to control pressure inside the core. Pressure and temperature will be measured along the core using pressure transducers and thermocouples and will be automatically recorded in a data acquisition system.

The core will be first dried and then vacuumed to completely remove air trapped inside the pore spaces. The rock will then be fully saturated with deaerated water, pressurized to 20 psig and heated to about 110°C using surface heaters. After pressures and temperatures along the core have stabilized, the pressure at the outlet end will rapidly be reduced to atmospheric pressure to initiate flashing of the liquid water. Pressures, temperatures and water production from the core will be continuously recorded in the data acquisition system during the entire flash experiment.

3.4.2 Modeling Results of Flash Experiments

The flash experiment was modeled using forward calculations in TOUGH2. Berea sandstone core, 10 cm. in length and two inches in diameter, was used and the initial conditions were set at 20 psig and 110°C. The flash process was modeled using a mass sink at one end of the core maintained at a constant pressure equal to atmospheric. The water saturation, pressure and temperature profiles with time and distance away from the outlet end of the core are plotted in Figures 3.15 to 3.20. Both linear and Corey relative permeability curves were used in the simulation runs. The endpoint water saturation was assumed to be equal to 0.2.

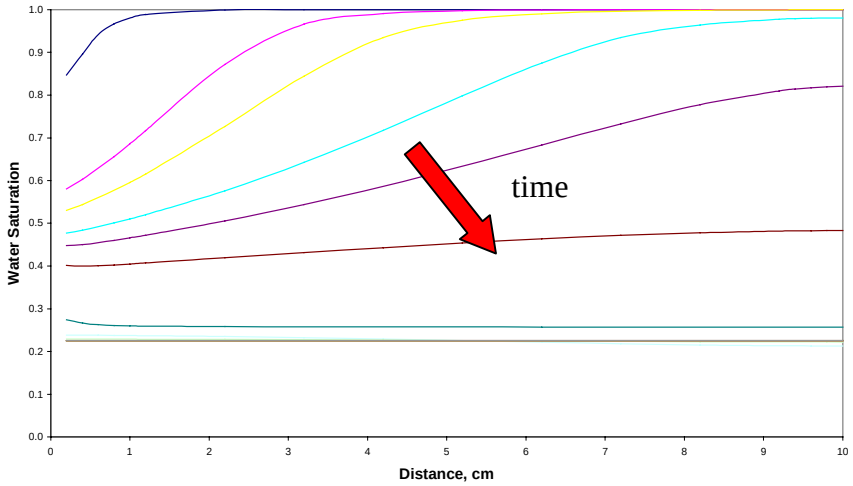

Figure 3.15: Water saturation profile with time and distance, using linear relative permeability curves.

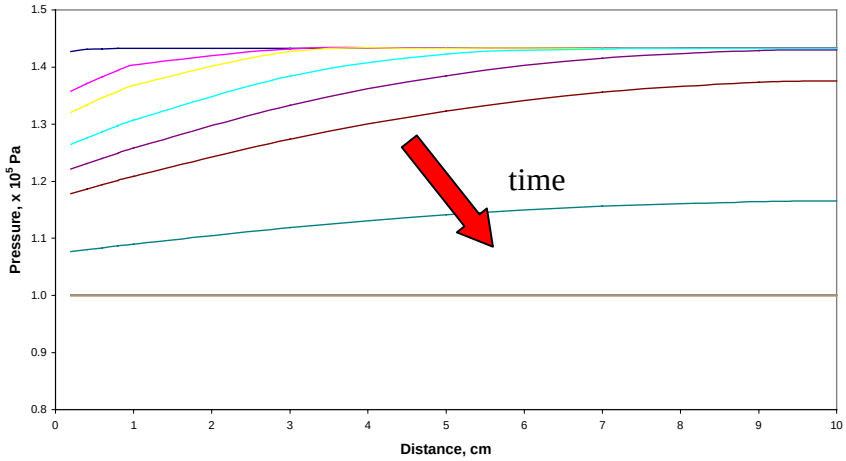

Figure 3.16: Pressure profile with time and distance, using linear relative permeability curves.

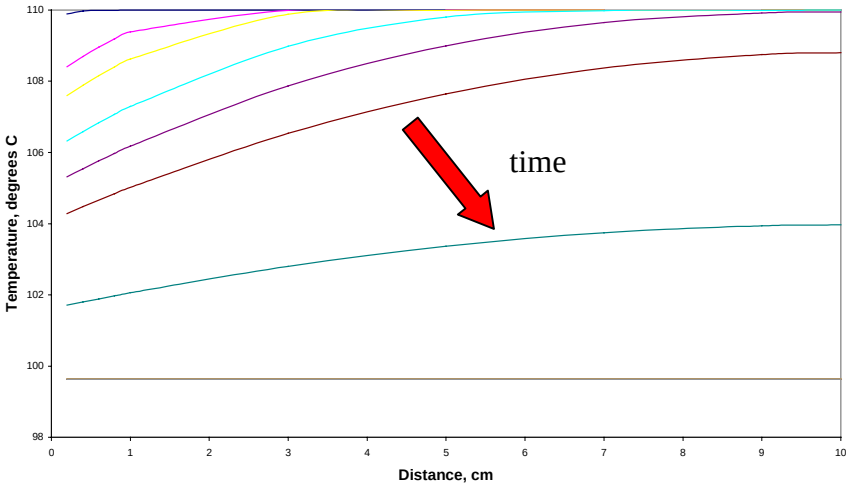

Figure 3.17: Temperature profile with time and distance, using linear relative permeability curves.

It is important to note that time increments used in the plots were logarithmically spaced. Most of the changes in the water saturation, pressure, and temperature took place in the first few seconds of the experiment and conditions have stabilized after a few minutes. Furthermore, water saturation throughout the core has gone down close to the assumed endpoint water saturation when linear relative permeability curves were used. On the other hand, water saturation does not reach the value corresponding to irreducible saturation if two-phase flow is assumed to be governed by Corey relative permeability curves.

3.4.3 Future Work

Future work will be directed towards further analyzing the modeling results as well as performing flash experiments using the current relative permeability experiment set-up.

Experimentation will confirm the modeling results and the field techniques proposed in the previous section of this report.

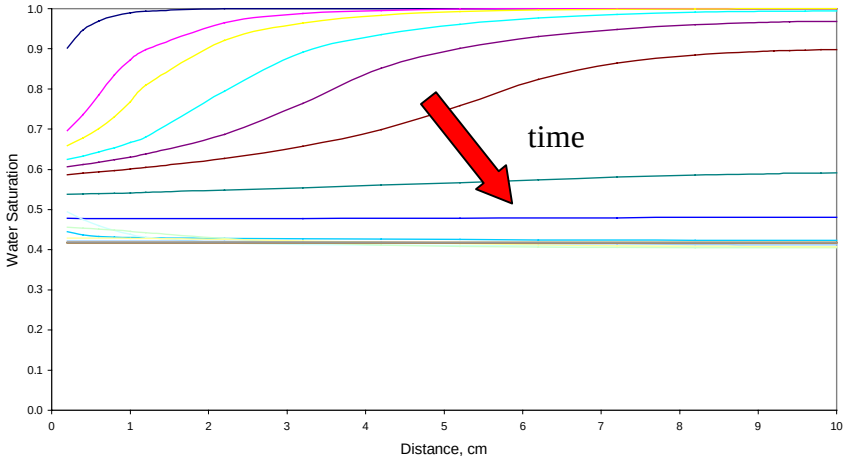

Figure 3.18: Water saturation profile with time and distance, using Corey relative permeability curves.

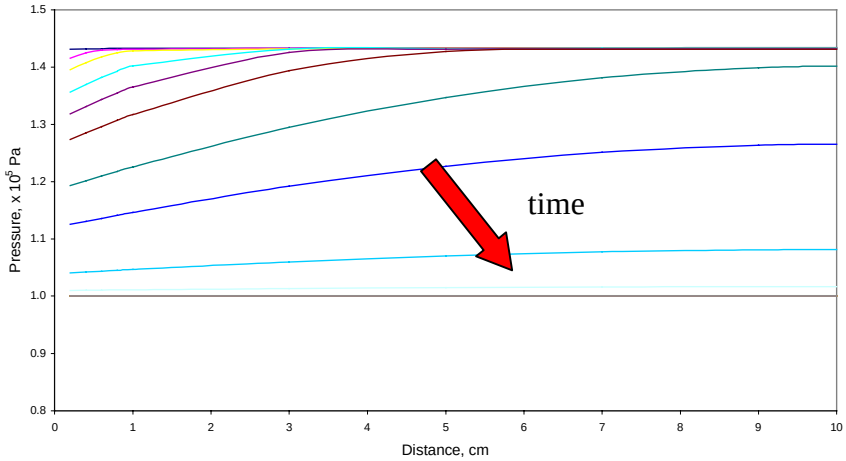

Figure 3.19: Pressure profile with time and distance, using Corey relative permeability curves.

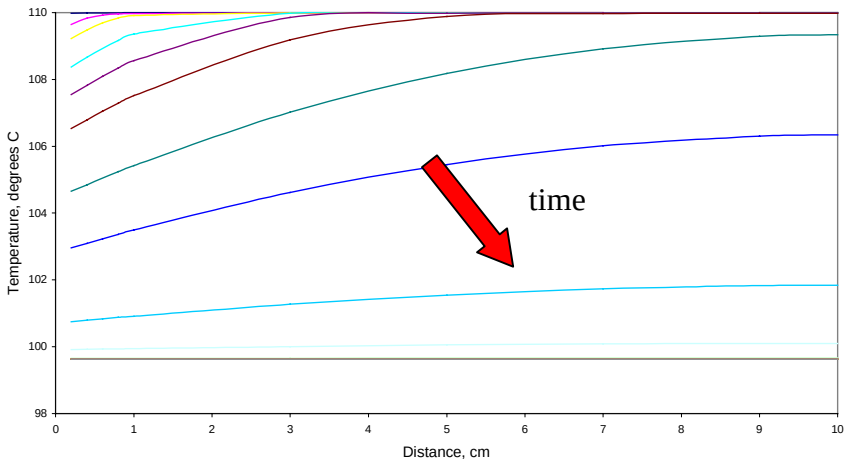

Figure 3.20: Temperature profile with time and distance, using Corey relative permeability curves.

4. STEAM-WATER CAPILLARY PRESSURE

This research project was conducted by Research Assistant Kevin Chow, Research Associate Kewen Li, and Professor Roland Horne. The final objective of this project is to develop a new method for calculating the capillary pressure in steam-water systems. Preliminarily, we studied the imbibition behavior of water into air-filled rocks at different initial water saturations in order to verify the method developed for calculating steam-water capillary pressure in porous media.

4.1 INTRODUCTION

The geothermal research program aims to determine the properties of steam production from underground rock, one aspect of which is the capillary pressure as a function of the steam saturation. This particular project focuses on the air-water system, as a way of stepping to the steam-water system that is present underground. The current stage seeks to explore the values and behavior of capillary pressures at various water saturations in Berea sandstone.

4.2 THEORY

In the January - March 1999 quarterly report, we reported a method to calculate air-water capillary pressure from the linear correlation between water imbibition rates and the reciprocal of imbibition recovery. The assumptions were that spontaneous imbibition is dominated by capillary pressure and that natural rock is water-wet in an air-water system, so spontaneous imbibition would occur upon contact between the rock and water. A derivation of a set of equations to calculate the capillary pressure follows in the report; this account will briefly summarize and derive those equations.

The combination of Darcy's equation and the definition of capillary pressure (p_g - p_w = p_c) yields:

$$v_w = \frac{k_w}{\mu_w}\left(\frac{\partial P_c}{\partial x} - \frac{\partial p_g}{\partial x} - \rho_w \cdot g\right) \tag{4.1}$$

where P_c is the capillary pressure, and p_g is the pressure of gas phase.

Assuming the gas mobility is infinite, the gas pressure gradient is estimated as:

$$\frac{\partial p_g}{\partial x} = -\rho_g \cdot g \tag{4.2}$$

where ρ_g is the gas density.

The combination of these last two equations yields:

$$v_w = \frac{k_w}{\mu_w}\left(\frac{\partial P_c}{\partial x} - \Delta\rho \cdot g\right) \tag{4.3}$$

where $\Delta\rho$ is the density difference between gas and water.

Based on experimental results, the water imbibition process is similar to a piston-like flow:

$$\frac{\partial P_c}{\partial x} = \frac{P_c}{x} \tag{4.4}$$

$$N_{wt} = A \cdot x \cdot \phi \cdot S_w \tag{4.5}$$

where A is the cross-sectional area, N_{wt} the accumulated volume of water imbibed into the core, ϕ the porosity, and S_w the water saturation behind the waterfront in the core. Combining the water imbibition rate equation,

$$Q = \frac{dN_{wt}}{dt} = A \cdot v_w \tag{4.6}$$

and Equation (4.3),

$$\frac{dN_{wt}}{dt} = a\frac{1}{\eta} - b \tag{4.7}$$

yields:

$$a = \frac{A \cdot k_w \cdot S_w}{\mu_w \cdot L} P_c \tag{4.8}$$

$$b = \frac{A \cdot k_w}{\mu_w} \Delta\rho \cdot g \tag{4.9}$$

and

$$\eta = \frac{N_{wt}}{V_p} \tag{4.10}$$

V_p is the pore volume of the core, L the length of the core, and η the cumulative fraction of gas recovered. We have shown that 'a' and 'b' are constants, and these equations are used to calculate capillary pressure. In this project, imbibition tests at different initial water saturations were performed.

A new equation was formulated in the July-September 1999 quarterly report. The N_{wt} is now

$$N_{wt} = A \cdot x \cdot \phi \cdot (S_w - S_{wi}) \tag{4.11}$$

where S_{wi} is the initial water saturation. The only equation needing modification follows as:

$$a = \frac{A \cdot k_w \cdot (S_w - S_{wi})}{\mu_w \cdot L} P_c \tag{4.12}$$

4.3 PROCEDURE

Two 10-cm long cylindrical Berea samples were cut with an electric circular saw. A vernier caliper was used for the length measurements. Water was used to keep the blade wet; consequently, the core sample got wet. The samples were then dried by heating in an air bath at various temperatures and times, as shown in Table 4.1.

Table 4.1: Heating history of core samples.

	Temp (°C)	Time (hrs)	Mass* of Core1 (g)	Mass* of Core2 (g)
1st Heating	75	48	397.52	395.04
2nd Heating	85	48	397.34	394.86

*masses after heating

The masses of the cores were measured on a balance, Mettler PE #1600, which has an accuracy of .01 gram and range of 0 to 1600 g. A thermocouple with a temperature reader was inserted into the oven to monitor the temperature. Care was taken to avoid cracking of the cores, caused by a sudden drop in temperature, by allowing the oven to cool to room temperature before opening the door of the oven.

Core holders were prepared. Plastic disks were equipped with rubber O-rings and metal tube fittings with Teflon tape. The core and these disks were then placed vertically to be wrapped with heat-shrinking tubing. A heat gun, with a temperature range of 600°F to 900°F, blew hot air onto the tubing and wrapped it tight onto the surface of the cores. The core is displayed in Figure 4.1.

Figure 4.1: Photograph of Core 1.

To measure the pore volume, a Welch Directorr #8915 Vacuum Pump was used to remove the air from the core. A schematic of the apparatus for measuring pore volume is shown in Figure 4.2. After vacuuming for about 2 hours at 60 millitorr, the core was fully saturated with water over a one-hour period. Following this, the excess water in the dead volume at both ends of the core was removed using a syringe, and the final weight was recorded. The dimensions of the cores were measured using a digital caliper (Model CD-8CS, manufactured by Mitutoyo Corp.) with an accuracy of 0.01mm. The porosity was calculated using this formula:

$$\phi = \frac{V_p}{V_t} \tag{4.13}$$

where V_t is the total volume of the core.

The pore volume, porosities, and dimensions of the cores are listed in Table 4.2.

Table 4.2: Core properties.

	Length (cm)	Diameter (cm)	Pore Volume (cc)	Porosity(vacuum method,%)
Core 1	10.006	4.962	45.18	23.3
Core 2	9.962	4.982	44.52	23.2

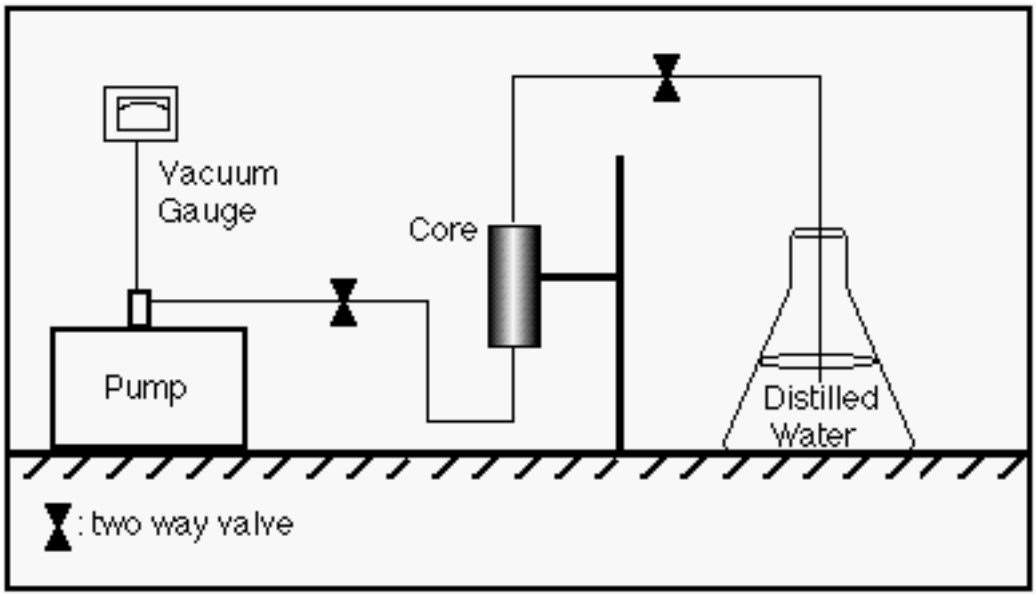

Figure 4.2: Vacuum method for measuring pore volume.

The cores were dried by first using air injection and then the vacuum. The apparatus used for the air injection consisted of compressed air and a Nupro flow-rate regulator. The differential pressure across the core samples was measured using a differential pressure transducer manufactured by Celesco Company; this transducer (Model DP30) has a linearity of 0.5% and a repeatability of 0.5% full scale. The diaphragm used in this study has a range from 0 to 10 psi. The schematic of the apparatus for air injection is displayed in Figure 4.3. Air was injected for a few hours at a pressure of about 7 psi.

For the evacuation, the same apparatus as shown in Figure 4.2 was used, but there were a few alterations. The changes consisted of putting a section of the tubing through a cold trap with dry ice (to freeze the moisture before it could enter the vacuum pump), and removing the water flask. The masses of the cores were measured again, after these steps, to check if they were dry.

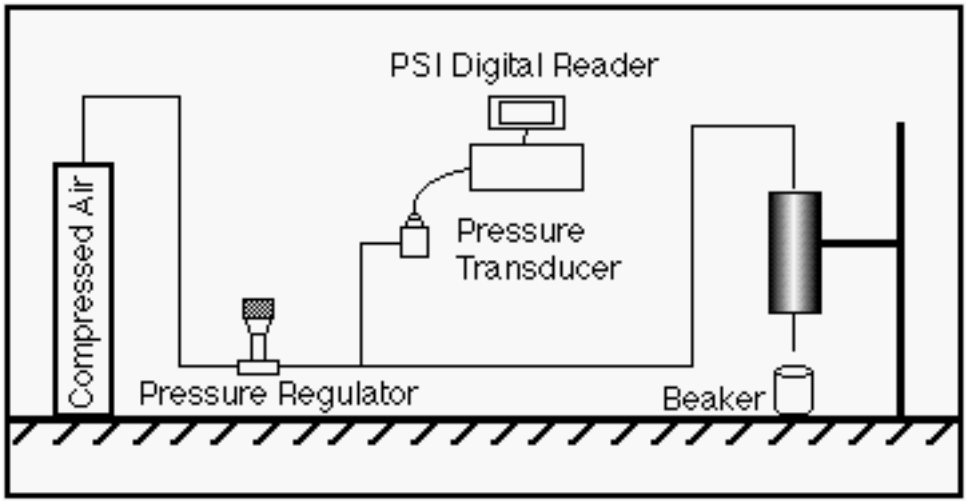

Figure 4.3: Air injection method for removing water from core.

Another way of calculating porosity is by scanning cross-sectional images, which can also be used to verify homogeneity within a sample. The CT Scanner used in this study was a Picker™ 1200 SX X-ray CT scanner with 1200 fixed detectors. The width of the scanning section was 10 mm, the tube current used in this study was 50 mA, and the energy level of the radiation was 140 keV. The acquisition time of one image is about 3 seconds while the processing time is around 40 seconds. The core was placed horizontally in the gantry of the X-ray CT machine, and five images of the cross-section, at 2-cm increments each, were taken. Figure 4.4 displays one of the CT scan images.

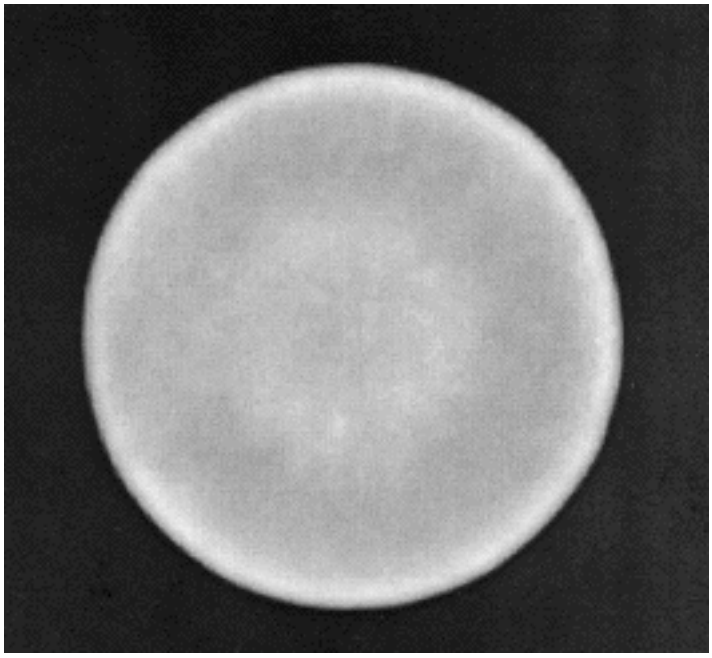

Figure 4.4: A CT image of the cross-section of the core.

The CT values of the cross-sections for each core and saturation, displayed in Table 4.3, were mostly consistent. This means that the distribution of fluids was fairly homogeneous throughout the cores. The heterogeneity of the core was negligible. The porosity was calculated again, using Equation (4.14):

$$\phi = \frac{CT_{wet} - CT_{dry}}{CT_{water} - CT_{air}} \tag{4.14}$$

Table 4.3(a): CT values of the air-saturated core.

	Position	Core 1	Core 2
CT, Sw=0%	2	1160	1158
	4	1158	1158
	6	1158	1159
	8	1158	1158
	10	1158	1157

Note: S_w = water saturation

Table 4.3(b): CT values of the core saturated with water.

	Position	Core 1	Core 2
CT, Sw=100%	2	1370	1370
	4	1370	1370
	6	1370	1371
	8	1369	1371
	10	1369	1371
Porosity (CT method, %)		21.1	21.2

Note: S_w = water saturation

Note that the values of the porosity of two core samples measured using the vacuum method were 23.3% and 23.2%, respectively (see Table 4.2). Table 4.3(b) shows that the values of porosity measured by the X-ray CT method are 21.1 and 21.2% for the same two core samples. This difference of porosity values may be explained by the incomplete removal of water in the core holders before the second weighing of the cores, as described earlier in this section. The graphs of the data from Table 4.3 are displayed in Figures 4.5 and 4.6.

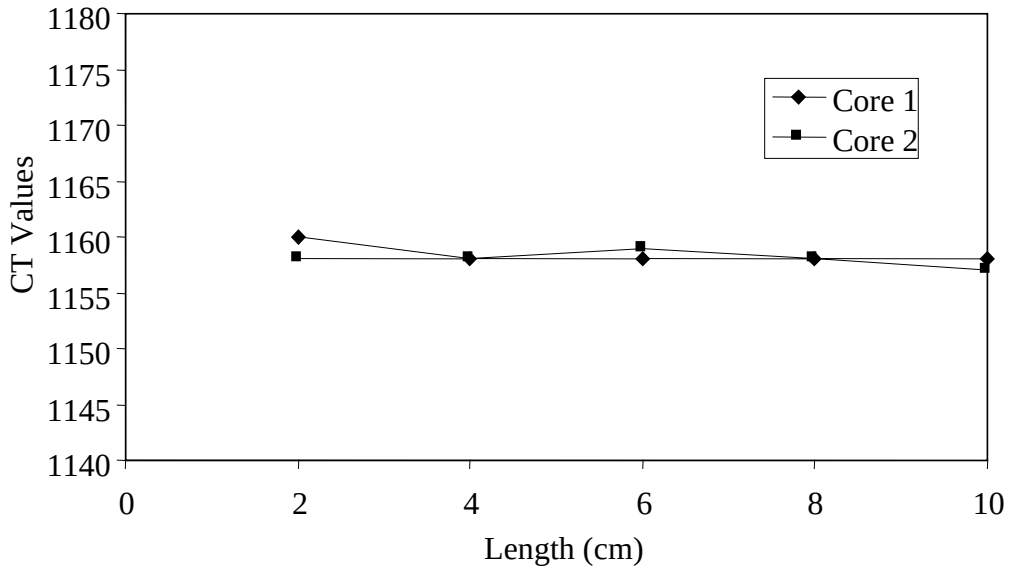

Figure 4.5: CT values along the dry core samples at S_w = 0%.

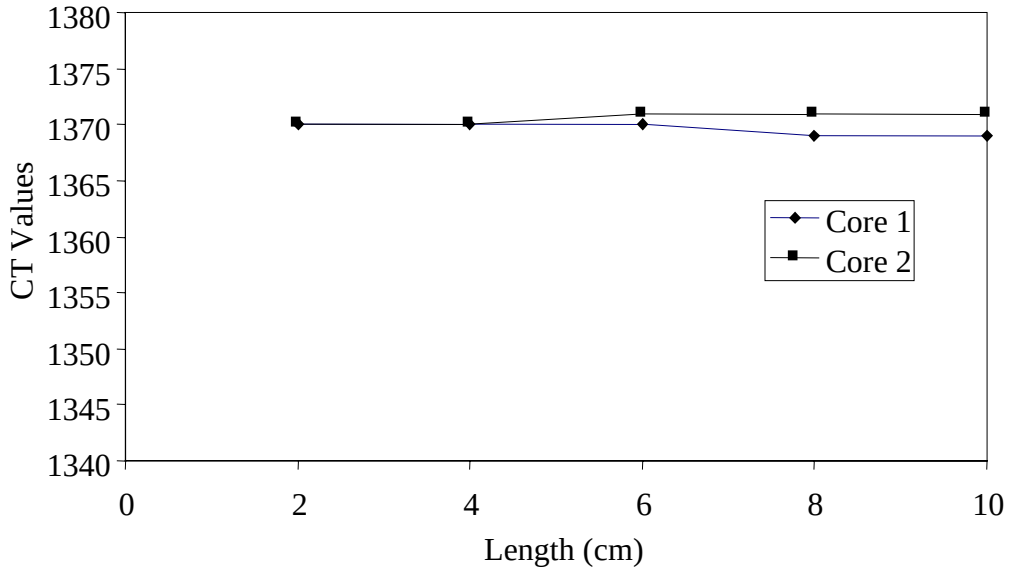

Figure 4.6: CT values along the saturated core samples at S_w = 100%.

Core #1 was set aside for future use, and preparations were made to establish the initial water saturation in Core #2. Distilled water was placed in a flask that was vacuumed to remove the air. This process lasted about 40 minutes, or until bubble formation was minimal, with vacuum pressure ranging from 23 to 29 inches of mercury. One of the plastic end plates in the core was removed by cutting the heat-shrink tubing just enough to pull out the end plate to conduct the water imbibition test. See Figure 4.7 for the shape of the bottom surface after removing the disk. The core was then hung under the Mettler balance by attaching a T-shaped tube fitting and a wire to the top end plate of the core. The distilled water was placed in a container, which sat on top of a lab jack. The balance

was connected to a computer with the programmable software LabView, Version 4.01, from the National Instrument Company. The water was raised up to about 2-3 mm above the bottom surface of the core, and LabView was initiated to acquire the data: time and weight. The schematic of the apparatus to perform water imbibition tests is shown in Figure 4.7.

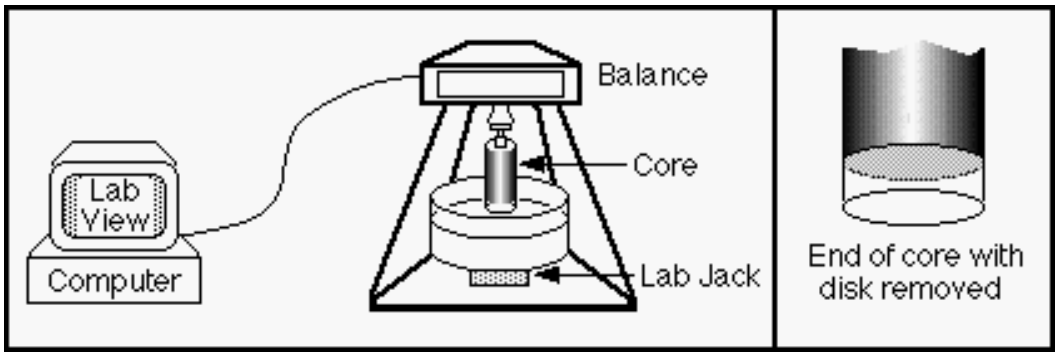

Figure 4.7: Apparatus for water imbibition test.

Care was taken to keep the core vertical. However, a bubble covered up part of the bottom surface of the core. The system was left standing for about three hours. The final water saturation by spontaneous water imbibition was measured by weighing and was about 60.2%.

A modification to the imbibition test apparatus was made to remove the bubble that appeared in the first imbibition test. A stainless steel tubing with an outside diameter of 1/8 inch was taped vertically to the side of the core; the end of the tubing was bent to the core bottom surface. Therefore, any air pockets could leave the inverted cup-like enclosure through the tubing. This modification was implemented in the remaining imbibition tests at different initial water saturations. There were no bubbles trapped at the bottom of the core during the experiments with this modification.

The water saturation of the core was then reduced to 50%, using the air injection method as shown previously in Figure 4.3, except that the core was turned horizontal. The purpose of this orientation was to attempt to lessen the effect of gravity on the water distribution. The pressure used for air injection ranged from 3 to 7psi, depending on the level of saturation and how quickly the core appeared to dry. The air was injected from either outlet or inlet, switching back and forth every 5 minutes or so. Care was taken to inject the same air pressure at both ends of the core for maximum uniformity.

Other ways of making sure the water in the core was homogeneously distributed included scanning cross-sections with the CT scanner and letting the core sit overnight. These two methods, including switching the end of injection, proved to be quite reliable. Therefore, after scanning the core at 40% water saturation and finding the water adequately homogeneous within the core, no more CT scans were performed for other initial saturations. The graph of water saturation versus position is shown in Figure 4.8.

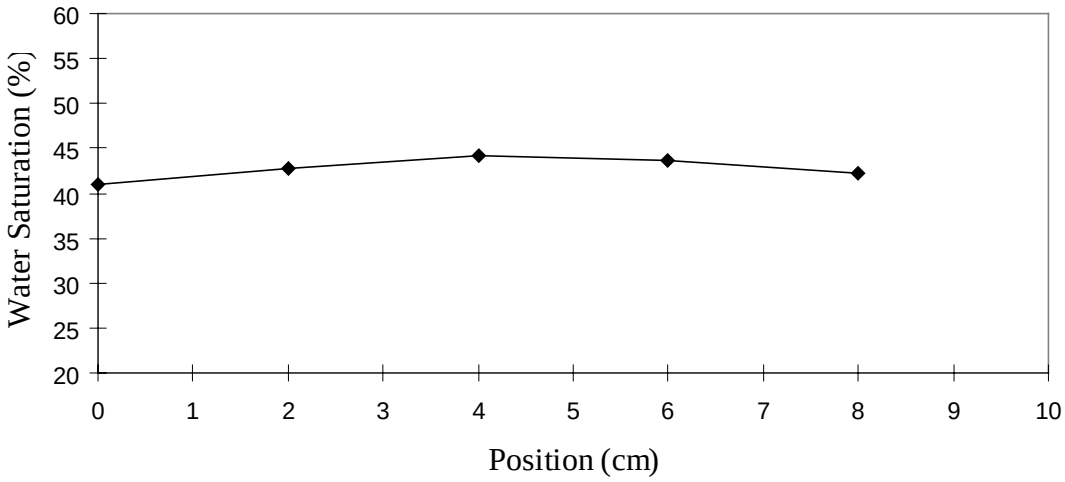

Figure 4.8: Water saturation vs. position.

The imbibition tests were performed at 40%, 30%, 20%, and 10% initial saturations. Due to the inconsistent results in the data of 10% water saturation, additional tests at 0% and 10% were executed. After the completion of these tests, the absolute permeability was measured, with the apparatus displayed in Figure 4.9.

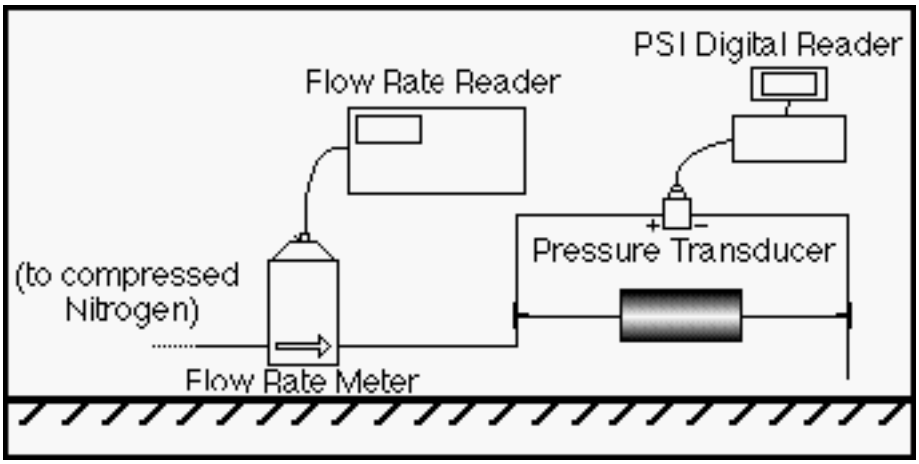

Figure 4.9: Schematic for permeability measurement.

The flow rate meter used was Matheson's Mass Flow Transducer, Model 200. The absolute permeability was measured to be about 500md.

4.4 RESULTS

Figure 4.10 shows the graph of water imbibed versus time for all water saturations. It is noted from the graph that the velocity of the water imbibition front increased quickly in the first 3 minutes or so, then gradually slowed as water was pulled up the core. The

graph of the experiment at initial saturation 10% veers from the trend; its velocity increases too slowly and levels off at a point far to the right of the graph's range. This leads us to suspect experimental error for this one run.

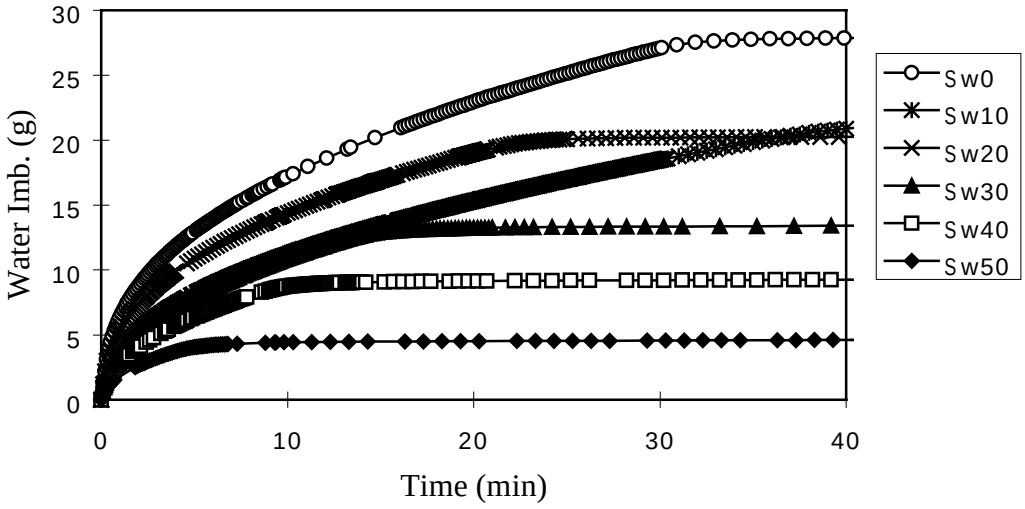

Figure 4.10: Plot of water imbibed vs. time.

A trend in this figure, from studying the shapes of the data series, is the flattening out of the graphs at certain times. These times are plotted against water saturation in Figure 4.11. There exists a linear relationship between the saturation and the flattening time.

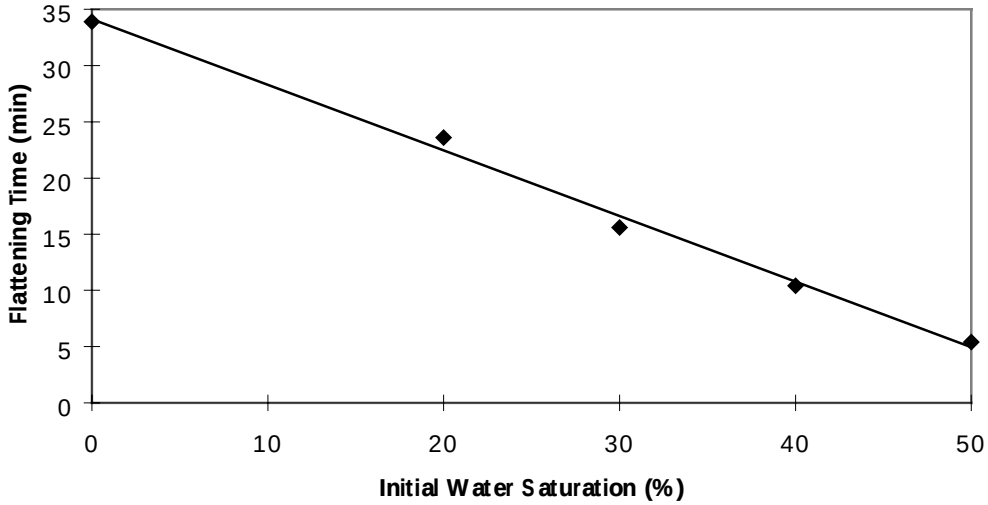

Figure 4.11: Flattening time (min) vs. initial water saturation.

Figure 4.12 displays the water imbibition rate with time. The steep decline of the imbibition rates show that the velocities level off within 4 minutes or so.

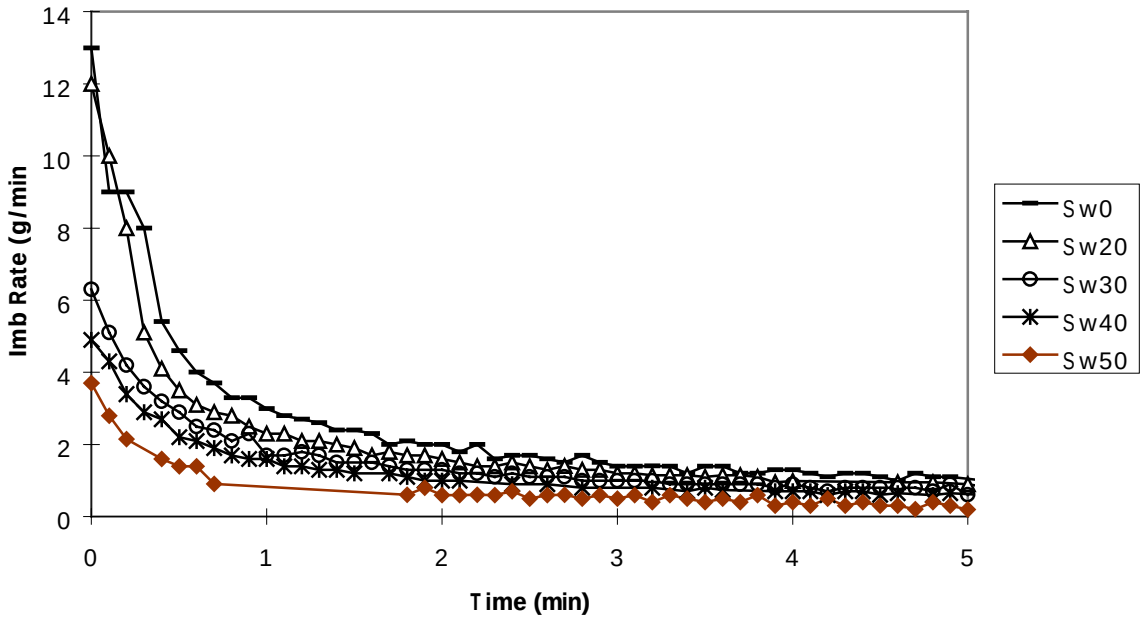

Figure 4.12: Imbibition rate (gm/min) vs. time.

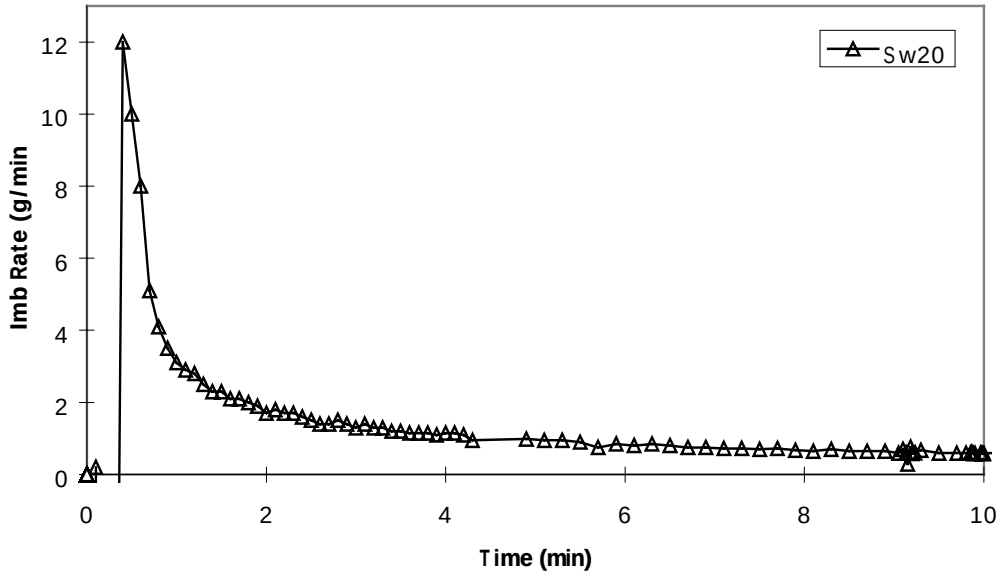

Figure 4.13: Imbibition rate vs. time for 20% saturation.

Using the graph in Figure 4.13, one can determine the initial time at which the water contacts the bottom surface of the core, as the calculations of capillary pressure depend on this determination. This contact time occurs at the cusp or maximum point of the graph, since the velocity is greatest when the water touches the core. Here, the maximum point for 20% saturation is the point at 12 g/min.

The graph of imbibition rate versus the pore volume divided by the water imbibed is displayed in Figure 4.14. It is noted in this Figure 4.that there is a linear correlation between the reciprocal of water imbibed and the imbibition rate, as predicted in the January - March 1999 quarterly report.

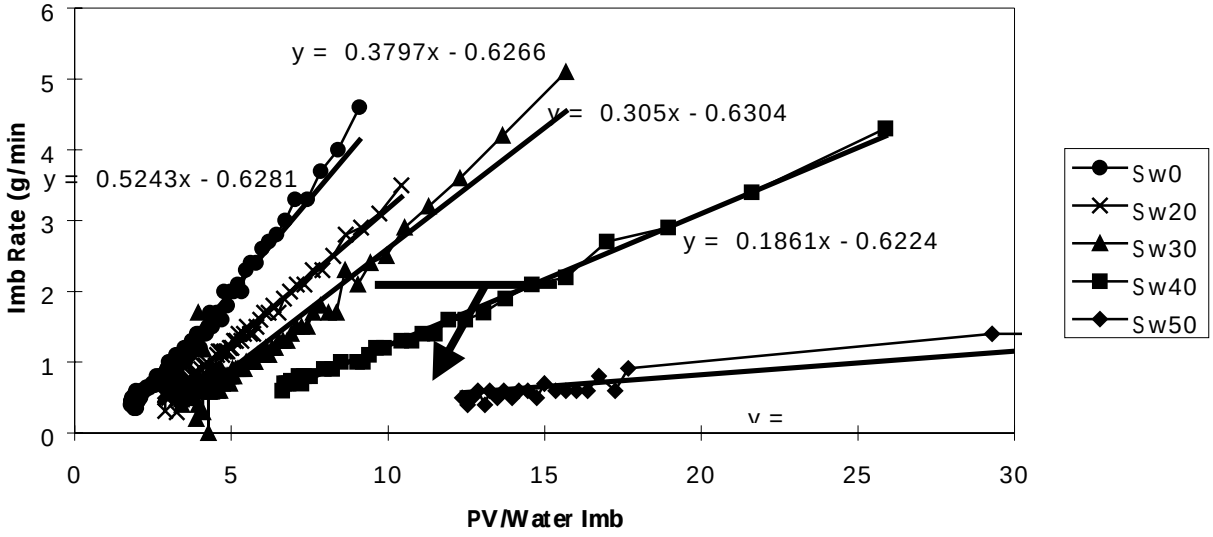

Figure 4.14: Imbibition rate vs. pore volume/water imbibed.

The capillary pressures, as calculated from Equations (7), (8), (9), and (12), at various initial water saturations are displayed in Figure 4.15 and Table 4.4.

Table 4.4: Capillary pressures as a function of water saturations.

Sw (%)	Pc (mm water column
0	138.13
10	66.112
20	151.22
30	152.04
40	131.81
50	91.343

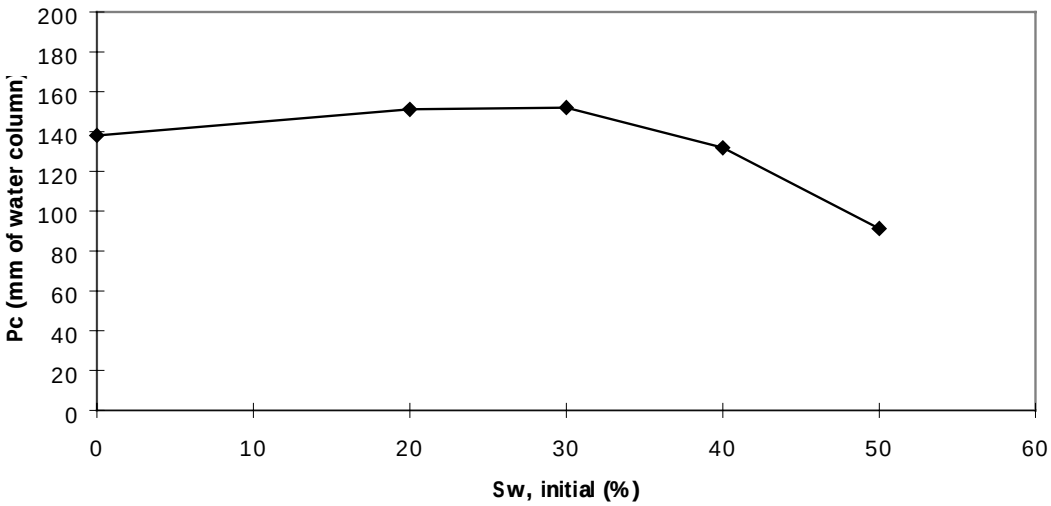

Figure 4.15: Capillary pressure versus initial water saturation.

The set of data for 10% saturation was not included in the charts and graphs, except in Figure 4.10, which was merely used to demonstrate the experimental error of the run at 10%. The inconsistency of the value at 10% in all the figures may be explained by the supposition that, in regards to Figure 4.15, there is a vertically oriented asymptotic boundary between 10% and 15% water saturations. The values obtained at 0% and 10% has been postulated as being jumps; in other words, they could be simulating imbibition behavior at 35% and 55%, respectively. Therefore, the data from the 10% saturation experiment has been omitted.

It can be seen in Figure 4.15 that the relationship between capillary pressure and initial water saturation does not look like the usual capillary pressure curves as measured by some other methods, for example, those by a porous-plate method or a mercury-injection method. The reason is under investigation.

4.5 CONCLUSIONS

Experimental data have confirmed that there is indeed a linear relationship between the imbibition rate and the fraction of water imbibed divided by the pore volume, even at different initial water saturations. This account has shown that the new method of calculating the capillary pressure may be feasible.

5. SLIP FACTOR IN GEOTHERMAL ROCKS

This research project is being conducted by Research Associate Kewen Li and Professor Roland Horne. The objective of is to measure the slip factor of geothermal rocks using an apparatus developed for the purpose.

5.1 SUMMARY

An apparatus to measure the permeability and slip factor of geothermal rocks has been developed. The intrinsic permeability of a rock from The Geysers geothermal field measured by nitrogen injection was about 0.56 md, mainly attributable to the fracture permeability; the slip factor was around 2.86 atm.

5.2 INTRODUCTION

It is known from our previous study (Li and Horne, 1999) that the effect of gas slippage on steam-phase relative permeability is significant in Berea sandstone samples. Few data of slip factor and gas-water relative permeability for geothermal rocks are available due to the extremely low porosity and permeability. Persoff and Hulen (1996) measured the permeabilities of four rocks from The Geysers ranging from 1.3×10^{-6} to 0.22 md. The high permeability value of 0.22 md was too high to represent the permeability of the matrix of the rock, presumably due to the contribution of the fractures. Persoff and Hulen (1996) used small rock samples, 2.5 cm in diameter and 5.0 cm long. Considering our intention ultimately to measure the gas-water relative permeability and the very low porosity of the rock from The Geysers field, we used a larger size rock sample. If the size of the rock is small, the pore volume will be small. A small pore volume is not good for the reliable measurement of gas-water relative permeability. The risk to use large size rock sample is that more fractures may be captured. However, the same problem exists even using small size rock sample as reported by Persoff and Hulen (1996), besides which it is clear that the presence of fractures will also govern the flow properties of the rocks within the reservoir itself.

The effect of slip factor on gas-phase relative permeability in geothermal rocks is not clear. As a preliminary step, we developed an apparatus to measure the permeability and slip factor of geothermal rocks with low porosity and permeability. This apparatus will be modified to measure gas-water relative permeability for geothermal rocks in the near future. The intrinsic permeability and the slip factor of a rock from The Geysers geothermal field have been measured by nitrogen injection this quarter.

5.3 EXPERIMENTS

The rock permeability was measured by injecting nitrogen at room temperature; the viscosity of nitrogen at a temperature of 20^{o}C is 0.018cp. We used a rock sample from The Geysers geothermal field at the depth of 1409.3m; its length and diameter were 4.70 cm and 6.91 cm, and the porosity was about 4.5%. We observed that there were some fractures in this rock, as shown in one of the X-ray CT images in Figure 5.1.

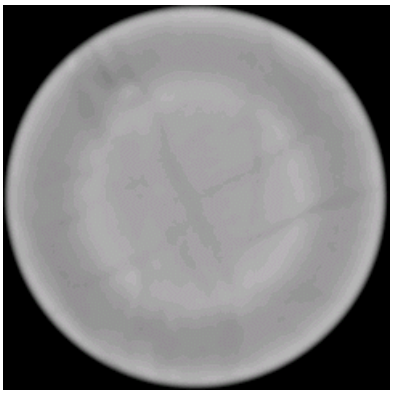

Figure 5.1: X-ray CT image of a rock from The Geysers geothermal field.

The CT-Scanner used was a Picker™ 1200 SX X-ray CT scanner with 1200 fixed detectors. The voxel dimension is 0.5 mm by 0.5 mm by 5 mm, the tube current used in this study was 50 mA, and the energy level of the radiation was 140 keV. The acquisition time of one image is about 3 seconds while the processing time is around 40 seconds.

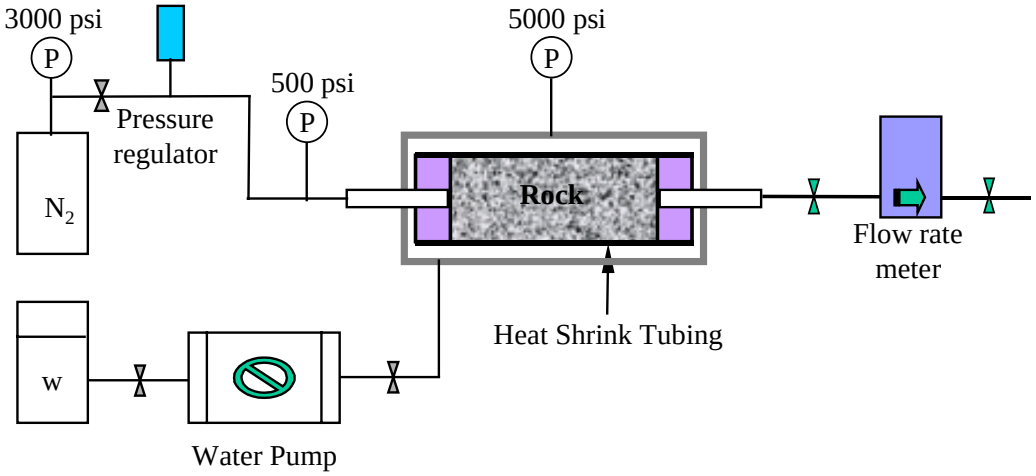

Figure 5.2: Schematic of apparatus for measuring steam slip factor.

Figure 5.2 shows a schematic of the apparatus to measure the permeability and slip factor of geothermal rocks with low permeability. A Hassler-type core holder made of stainless-steal was designed for flow tests at a high pressure up to 5000psi (see Figure 5.2).

The rock sample was machined carefully to make sure that the two end faces of the rock were flat and parallel to each other. The rock was wrapped with heat-shrink tubing since the diameter of the sample was not standard. There was a leak from the confining pressure system (annular space between the core holder and the heat-shrink tubing) to the pore pressure system. The leak problem was solved using a custom-made rubber sleeve.

The flow rate of nitrogen was measured by a mass-flow transducer (also a flow rate controller) manufactured by Matheson Company. This mass flow rate meter and

controller (Model 8272-MF200) has an accuracy of 1% over a range from 0 to 200 ml/min. The calibration curve of flow rate for this transducer using nitrogen is shown in Figure 5.3. After the first experiment, it was found that the range of the flow rate was not sufficient. Therefore another flow rate transducer made by the same company but with a wider range from 0 to 2000 ml/min was used to repeat the measurements. The calibration curves of flow rate for this mass flow transducer using both air and nitrogen are shown in Figure 5.4. There is almost no difference between the flow rates using air and nitrogen. In Figures 5.3 and 5.4 the x-axis represents the flow rates read or set on the controller for the mass flow transducer and y-axis the flow rates measured using a stop watch and the volume of water displaced by gas in a vertical glass cylinder at room temperature. The flow rates of nitrogen at room temperature were calibrated using the equations shown in Figures 5.3 and 5.4.

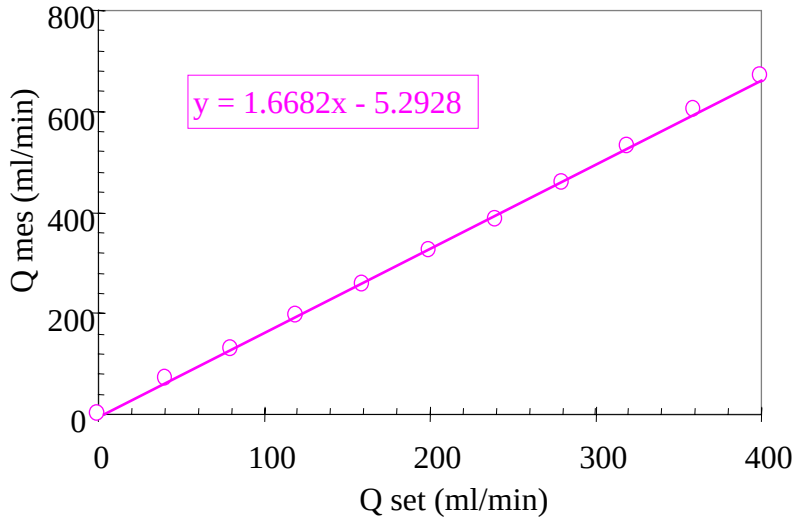

Figure 5.3: Calibration of flow rate for mass controller and transducer (Model 8272-MF200).

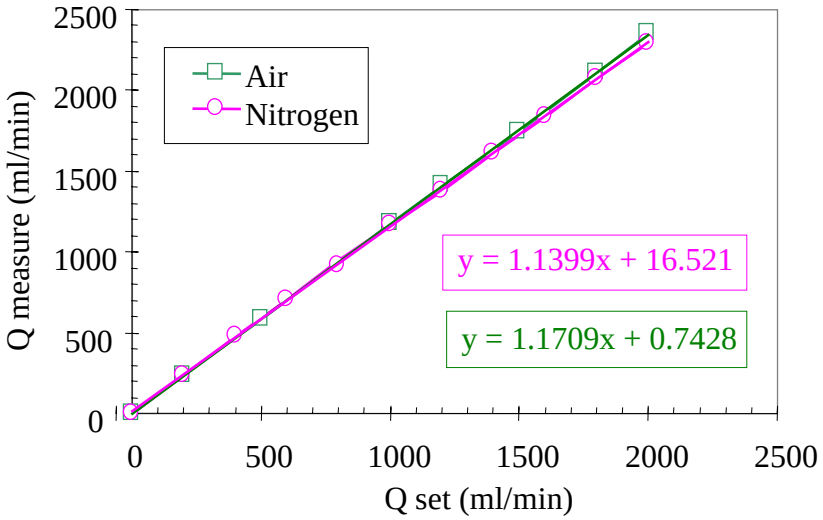

Figure 5.4: Calibration of flow rate for mass controller and transducer (Model 8272-MF2000).

All the pressures were measured using gauges with an accuracy of about 1%. The confining pressure could be applied either by a water pump or by compressed nitrogen. For convenience, the compressed nitrogen was used for low pressure and the water pump for high pressure.

The core sample was dried by heating to a temperature of 110^{o}C until its weight did not vary during eight hours. The core was then assembled in the apparatus after it was cooled down, as shown in Figure 5.2. Following that, a leak test was conducted for the whole system. Following that, nitrogen was injected into the core at different pressures to measure the permeability and the slip factor of the rock sample.

5.4 RESULTS

The permeability and the slip factor of the rock sample were first measured at a confining pressure of about 400 psi using the flow rate transducer (Model 8272-MF200) with a range of flow rate from 0 to 200 ml/min. The results are shown in Figure 5.5. The x-axis in Figure 5.5 represents the average pore pressure in the core sample and y-axis the permeability of the rock measured at different average pore pressures. The intrinsic permeability of this rock sample calculated using the values measured at different test mean pressures is about 0.6 md. At first we suspected that the permeability value of 0.6 md was too high. Therefore we repeated the measurements over a wider mean pressure range using another flow rate transducer (Model 8272-MF2000) with a range from 0 to 2000 ml/min. In order to make sure that there was no gap between the rock side surface and the heat-shrink tubing, the confining pressure was increased from 400 psi to about 600 psi. The intrinsic permeability of this rock sample calculated using the experimental data from the repeated measurements was about 0.56 md as shown in Figure 5.5; the slip factor was around 2.86 atm. It can be seen from Figure 5.5 that the results from the two tests are closely consistent with each other. The permeability value of 0.56 md might seem too high to represent the permeability of the matrix of the rock from The Geysers geothermal field, since most of the flow may be contributed by the permeability of the fractures. Persoff and Hulen (1996) reported a similar permeability value of 0.22 md for a rock from The Geysers geothermal field. They converted this permeability value to an effective fracture aperture of about 1.6 μm.

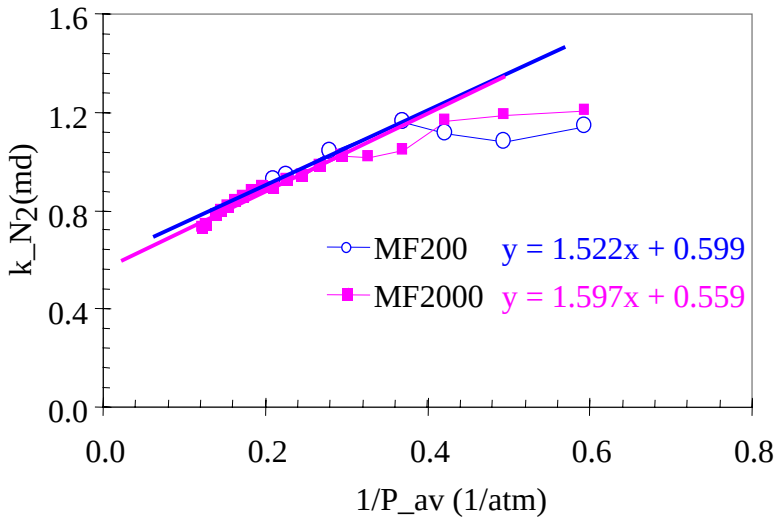

Figure 5.5: Permeability and slip factor of a rock from The Geysers.

The fact of the repeatability of experimental results shown in Figure 5.5 and the consistency with the results reported by Persoff and Hulen (1996) shows that the apparatus developed in this work could be used successfully to measure the permeability and slip factor for geothermal rocks with low permeability. This apparatus will also be utilized to measure the gas-water relative permeability at high pressures for geothermal rocks with some modification. Gas-phase relative permeability (k_{rg}) of geothermal rocks is subject to the correction of Klinkenberg slippage effect by using the slip factor measured in this study because there is a significant effect of gas slippage in low permeable rocks.

5.5 CONCLUSIONS

Based on the current quarter's results work, the following conclusions may be drawn:

1. The apparatus developed in this work was used successfully to measure the permeability and slip factor for geothermal rocks with low permeability.
2. The intrinsic permeability of the rock sample from The Geysers geothermal field was about 0.56 md, a value that represents the permeability of both fractures and matrix in the rock.
3. The slip factor of the rock measured at room temperature and a confining pressure of 600 psi was around 2.86 atm.

5.6 FUTURE WORK

The next step is to modify the apparatus to be able to measure gas-water relative permeability of the rock.

6. EXPERIMENTAL INVESTIGATION OF STEAM AND WATER RELATIVE PERMEABILITY ON SMOOTH WALLED FRACTURE

This project is being conducted by Research Assistant Gracel P. Diomampo, Research Associate Kewen Li and Prof. Roland Horne. The goal is to gain better understanding of steam-water flow through fractured media and determine the behavior of relative permeability in fractures.

6.1 BACKGROUND

Geothermal reservoirs are complex systems of porous and fractured rocks. Complete understanding of geothermal fluid flow requires knowledge of flow in both types of rocks. Many studies have been done to investigate steam and water flow through porous rocks. This is not the case for multiphase flow in fractures. Only a few published data are available most of which have been done for air-water system or for water-oil systems. Earliest is Romm's (1966) experiment with kerosene and water through an artificial parallel-plate fracture lined with strips of polyethylene or waxed paper. Romm found a linear relationship between permeability and saturation, $S_w = k_{rw}$, $S_{nw} = k_{rnw}$ such that $k_{rw}+k_{rnw} = 1$. Pan et al. (1996) performed a similar experiment with an oil-water system but arrived at conflicting results. Significant phase interference was observed such that $k_{rw} + k_{rnw} < 1$. Both studies, however, conclude that residual saturations are zero such that a discontinuous phase can flow as discrete units along with the other phase.

In an attempt to develop a relationship between fracture relative permeability and void space geometry, Pruess and Tsang (1990) conducted numerical simulation for flow through rough-walled fractures. Their study shows the sum of the relative permeabilities is less than 1, residual saturation of the nonwetting phase is large and phase interference is greatly dependent on the presence or absence of spatial correlation of aperture in the direction of flow. Persoff et al. (1991) did experiment on gas and water flow through rough-walled fractures using transparent casts of natural fractured rocks. The experiment showed strong phase interference similar to the flow in porous media. Data of Persoff (1991) and Persoff and Pruess (1995) for flow through rough walled fracture were compared in Horne et al. (2000), as shown in Figure 6.1.

Presently, the mechanism of flow and the characteristic behavior of relative permeability in fractures are still undetermined. Issues such as whether a discontinuous phase can travel as discrete units carried along by another phase or will be trapped as residual saturation as in porous medium are unresolved. The question of phase interference i.e. is the relative permeability curve against saturation an X-curve, Corey or some other function is still unanswered. The main objective of this study is to contribute to the resolution of these issues. Experiments on flow through smooth-walled fractures will be done first for air-water with the aim of establishing a reliable methodology for flow characterization and permeability calculation. Then these experiments will be done with a steam-water system; and with rough-walled fractures.

6.2 EXPERIMENTAL APPARATUS AND MEASUREMENT TECHNIQUES

Currently, an apparatus is being prepared for experiments in air-water flow. The apparatus consists of a 183 cm length of horizontal glass plate on top of an aluminum plate. The aperture is dictated by a 0.2 mm thick tape inserted in between the glass and aluminum plate along the boundaries and in three columns along the flow area. The sides of the plates are sealed together with an aquarium sealant to ensure no leakage of either liquid or gas. Horizontal slits in the ends of the metal plate serve as entry and exit points for the fluids. Gas flow will be controlled through a flow regulator, and maintaining a constant head in the water reservoir will control water flow rate. Figure 6.2 is a schematic diagram of this set-up.

Pressures will be read through manometers located at each end of the metal plate through tees in the outlet and inlet tubing. Water flow rate will be measured by collection and weighing of the outgoing stream. Gas flow rate can be read directly in the flow regulator. Saturation will be computed by measuring the area that each phase occupies. This will be done by taking digital photos of sections of the plates, once pressure and flow has stabilized. These sections will be chosen far enough from the ends of the plates to prevent end effects. The photographs will then be processed in a Matlab program that will plot the color histogram and calculate the areas under these histograms to determine the fractions occupied by each of the two phases. Figure 6.3 shows an example of a simple black and white scanned image, and the color histogram produced by the program. The calculated saturation was 57% with range of 0 to 100 on the color scale taken as black and 200 to 260 as white.

Pan et al. (1996) also used this technique for measurement of saturation. This study noted that the sources of error in this technique were the quality of the photographs and the water film adsorbed on the surfaces of the plates with the latter being of minimal effect. Good quality photographs are the ones with clear distinction between the gas and liquid phases. Water-soluble dyes will be used to enhance visualization of phase boundaries.

6.3 FUTURE WORK

Single-phase experiments at three different water flow rates will be done to determine the average aperture of the apparatus. Aperture will be calculated based on the cubic law:

$$a = -\left(\frac{12\mu_i Q_i L}{W \Delta p_i} \right)^{1/3} \tag{6.1}$$

with i representing the water phase, μ the viscosity , Q the flow rate, Δp the steady-state differential pressure, W and L the width and length of the fracture.

Then, the two-phase experiment with water and nitrogen gas will proceed with each run gradually increasing in nitrogen saturation. Pan et al. (1996) discussed two approaches in data analysis: the porous medium approach where Darcy's law is used and the homogeneous single-phase approach where the system is treated as a single-phase pipe

flow. The choice as to approach is more applicable will depend on the flow characteristics observed in the experiments. The results of these experiments will be compared to previous studies and the apparatus modified for steam-water flow and rough-walled fracture surfaces.

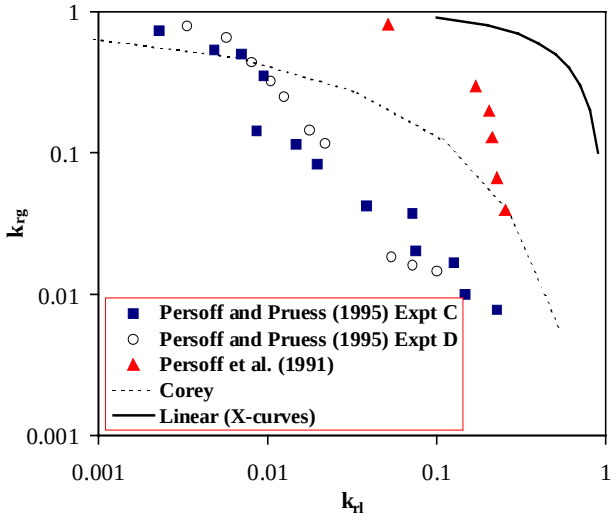

Figure 6.1: Some measurements of air-water relative permeabilities in rough-walled fractures (graph from Horne et al., 2000).

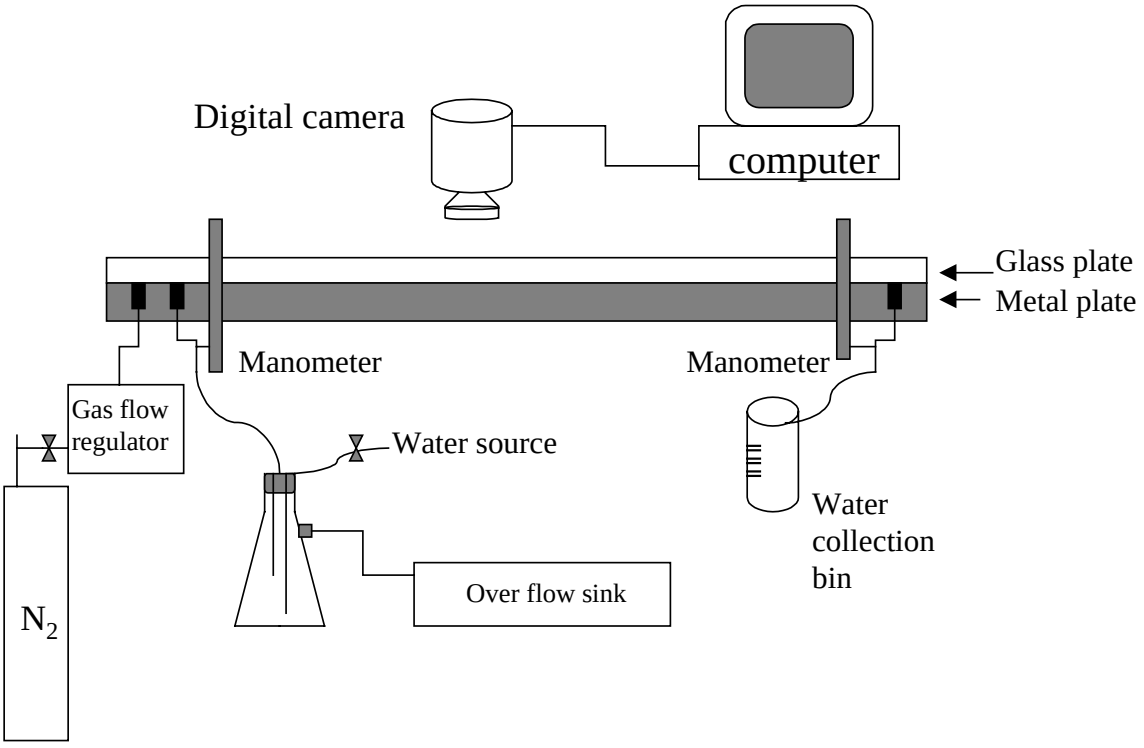

Figure 6.2: Apparatus for air and water flow through smooth walled fractures.

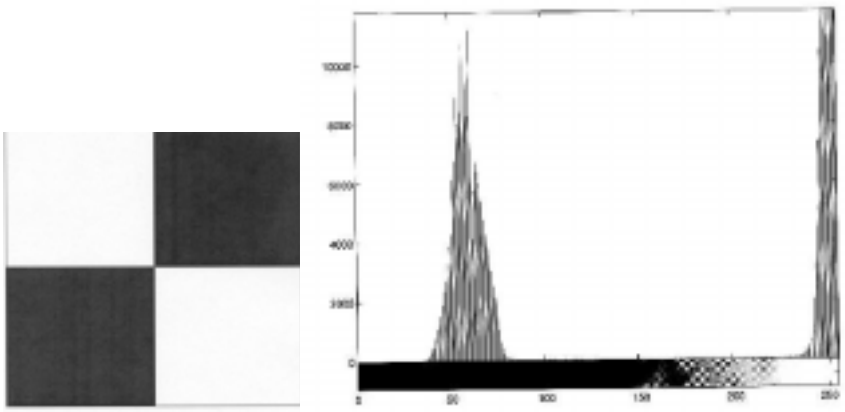

Figure 6.3: Sample image, and the corresponding histogram used to test the saturation calculation.

7. DEVELOPMENT OF A VOGEL-TYPE EQUATION FOR PRODUCTIVITY INDEX OF GEOTHERMAL WELLS

This project was undertaken by Research Assistant Brian A. Arcedera and Prof. Roland Horne. The goal was to develop dimensionless inflow performance curves for geothermal wells that are valid for a range of formation properties, initial conditions, and different stages of the well's production life. Use of these dimensionless curves would allow generation of deliverability curves from fewer data.

7.1 BACKGROUND

In 1968, Vogel presented an empirical formula to describe the inflow performance relationship (IPR) for solution-gas drive reservoirs. Using a computer program to compute IPR using two-phase theory, several simulated solution-gas drive reservoirs were examined. These reservoirs covered a wide range of conditions including differences in crude oil characteristics, differences in reservoir relative permeability, as well as the effects of well spacing, fracturing, and skin restrictions. Dimensionless IPR curves were computed from the simulated IPR curves by dividing the pressure for each point on an IPR curve by the maximum or shut-in pressure for that particular curve, and by dividing the corresponding production rate by the maximum producing rate for the same curve. Vogel found that plotting the IPR in dimensionless form produced curves that were remarkably similar. The equation that gave a reasonable empirical fit to this set of curves was:

$$\frac{q_o}{q_{o,\max}} = 1 - 0.2\frac{p_{wf}}{\overline{p}_r} - 0.8\left(\frac{p_{wf}}{\overline{p}_r}\right)^2 \quad \text{.....(7.1)}$$

where q_o is the producing rate corresponding to a given well intake pressure p_{wf}, p_r is the corresponding reservoir pressure, and $q_{o,max}$ is the maximum producing rate (Figure 7.1).

Figure 7.1: Vogel's inflow performance relationship for solution-gas drive reservoirs.

Vogel's IPR was extended further in 1996 by Wiggins et al. who presented a theoretical basis for the equation based on the physical nature of the multiphase flow system. The

resulting analytical IPR was derived from a Taylor series expansion of the multiphase flow equations. This analytical IPR, unlike Vogel's IPR, did not have a universal coefficient for the pressure terms. The coefficients of the pressure terms in the analytical IPR were functions relative permeability, fluid viscosity, and formation volume factors.

The analytical IPR can be used to develop reservoir-specific dimensionless IPR curves. The dimensionless IPR can in turn be used to develop deliverability curves for any well at any point in its producing life using a single data measurement. It is with this same end in mind that this project was undertaken. It was hoped that a similar dimensionless IPR can be developed and used for geothermal reservoirs.

7.2 PREVIOUS RELATED WORK

A review of related literature has turned up papers by Iglesias and Moya (1990) and Moya et al. (1998) discussing the development, use, and testing of geothermal inflow performance curves. The mass productivity reference curve can be expressed as:

$$W^* = 1.00 - 0.256P^* - 0.525P^{*2} - 0.057P^{*3} - 0.162P^{*4} \quad \text{.....(7.2)}$$

The thermal productivity reference curve on the other hand, can be expressed as:

$$Pow^* = 0.918W^* + 0.082W^{*2} \quad \text{.....(7.3)}$$

where W is the mass flow rate, P is the pressure, Pow is the heat flow rate (mass flow rate x enthalpy), $W^* = W/W_{max}$, $P^* = P/P_{max}$, and $Pow^* = Pow/Pow_{max}$ (Figure 7.2). These curves allow the computation of the complete inflow curve of a well from a single bottomhole measurement of mass flow rate, pressure, and specific enthalpy (W,P,h); or a single wellhead measurement (W,P,h), together with the use of a wellbore simulator.

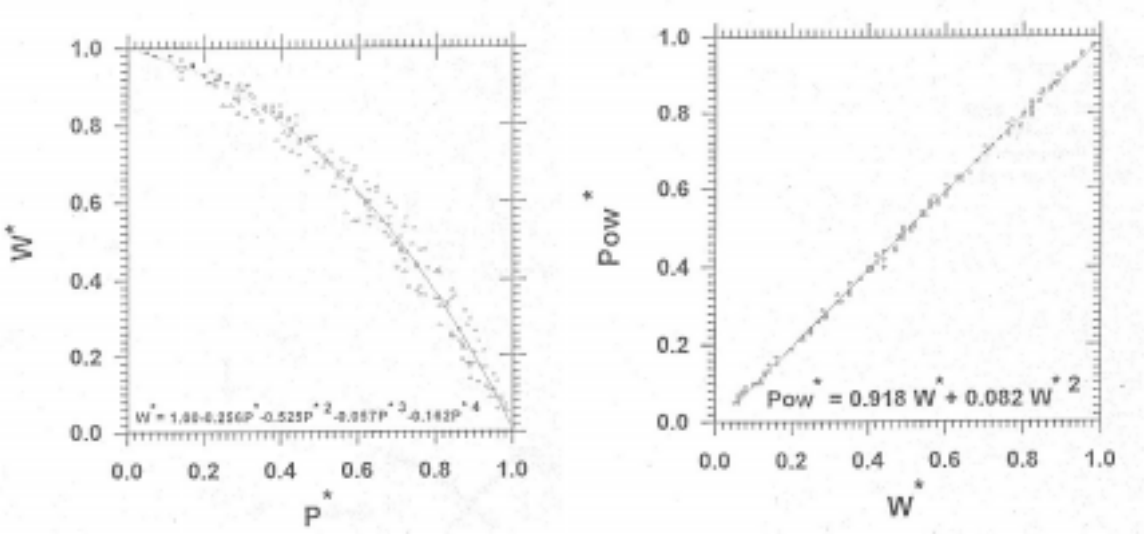

Figure 7.2: Dimensionless reference curves of the inflow performance for geothermal wells. (from Iglesias and Moya, 1990)

7.3 CONCLUSION

Based on the review of related literature, a dimensionless inflow performance relationship for use in geothermal reservoirs has already been developed in Mexico.

8. REFERENCES

Ambusso W., Satik C., and Horne R.N.: "A Study of Relative Permeability for Steam-Water Flow in Porous Media", Proceedings of 21st Workshop on Geothermal Reservoir Engineering, Stanford University, Stanford, California (1996).

Amyx, J., Bass, D., Jr., and Whiting, R.: *Petroleum Reservoir Engineering: Physical Properties*, McGraw-Hill Company, New York, 1960.

Grant, M.A.: "Water Content of the Kawah Kamojang Geothermal Reservoir", *Geothermics*, **8**, (1979), 21-30.

Guerrero, M., Satik, C., Finsterle, S., and Horne, R.N.: "Inferring Relative Permeability From Dynamic Boiling Experiments", Proceedings of 23rd Workshop on Geothermal Reservoir Engineering, Stanford University, Stanford, California (1998).

Horne, R.N.: Notes on Geothermal Reservoir Engineering, Stanford University, Stanford, California (1991).

Horne, R.N., Satik, C., Mahiya, G., Li, K., Ambusso, W., Tovar, R., Wang, C., and Nassori, H.: "Steam-Water Relative Permeability", to be presented at the World Geothermal Conference, Japan, May 2000.

Iglesias, E.I., and Moya, S.L.: "Geothermal inflow performance relationships", Geothermal Resources Council Transactions, Vol. 14, Part II, (1990), 1201-1205.

James, C.R.: "Wairakei and Larderello: Geothermal Power Systems Compared", *New Zealand Journal of Science and Technology*, Volume 11, (1968), 709-719.

Li, K., and Horne, R.N.: "Accurate Measurement of Steam Flow Properties", *GRC Trans.* **23** (1999).

Mahiya, G. and Horne R.N.: "Measurements of Steam-Water Relative Permeability", Stanford Geothermal Program Quarterly Report April–June 1998, Stanford University, Stanford, California.

Moya, S.L., Aragon, A., Iglesias, E., and Santoya, E.: "Prediction of mass deliverability from a single wellhead measurement and geothermal inflow performance reference curves" *Geothermics*, **27**, No. 3, (1998), 317-329.

Nathenson, M.: "Some Reservoir Engineering Calculations for the Vapor Dominated System at Larderello, Italy", U.S. Geological Survey Open-file Report 75-142, April 1975.

Pan, X., Wong, R.C., and Maini, B.B.: "Steady State Two-Phase Flow in a Smooth Parallel Fracture", presented at the 47th Annual Technical Meeting of the Petroleum Society in Calgary, Alberta, Canada, June 10-12, 1996.

Persoff, P. and Hulen, J.B.: "Hydrologic Characterization of Four Cores from The Geysers Coring Project", Proceedings of 21st Workshop on Geothermal Reservoir Engineering, Stanford University, Stanford, California (1996).

Satik, C.: "Experiments of Boiling in Porous Media", Proceedings of 22nd Workshop on Geothermal Reservoir Engineering, Stanford University, Stanford, California (1997).

Satik, C.: “A Measurement of Steam-Water Relative Permeability”, Proceedings of 23rd Workshop on Geothermal Reservoir Engineering, Stanford University, Stanford, California (1998).

Persoff, P., and Pruess, K.: "Two-Phase Flow Visualization and Relative Permeability Measurement in Transparent Replicas of Rough-Walled Fractures", Proceedings, 16th Workshop on Geothermal Reservoir Engineering, Stanford University, Stanford, CA, Jan. 23-25, 1991, 203-210.

Pruess, K., and Tsang, Y.W.: "On Two-Phase Relative Permeability and Capillary Pressure of Rough-Walled Rock Fractures", *Water Resources Research* **26** (9), (1990), 1915-1926.

Vogel, J.V.: “Inflow Performance Relationships for Solution-Gas Drive Wells”, *Journal of Petroleum Technology*, (Jan 1968), 83-92.

Wiggins, M.L., Russell, J.E., and Jennings, J.W.: “Analytical Development of Vogel-Type Inflow Performance Relationships”, *SPE Journal*, (Dec 1996), 355-362.